A flexible photoacoustic retinal prosthesis

Audrey Leong[†], Yueming Li[†], Thijs R. Ruikes[†], Julien Voillot, Yuhao Yuan, Guo Chen, Clémence Bradic, Arnaud Facon, Chakrya-Anna Chhuon, Corentin Joffrois, Gilles Tessier, Marion Cornebois, Julie Dégardin, Jean-Damien Louise, Ji-Xin Cheng*, Chen Yang*, Hélène Moulet[#]*, Serge Picaud[#]*.
† equal contributions, # equal contributions

A. Leong, T.R. Ruikes, C. Bradic, C., Joffrois, G. Tessier, M. Cornebois, J. Dégardin and S. Picaud*
Sorbonne Université, CNRS, INSERM, Institut de la Vision, F-75012 Paris, France
Email: serge.picaud@inserm.fr

Y. Li, Y. Yuan, G. Chen
Department of Electrical and Computer Engineering,
Boston University,
Boston, MA, 02215, United States

J-X Cheng*
Department of Electrical and Computer Engineering and Department of Biomedical Engineering,
Boston University,
Boston, MA, 02215, United States
Email: jxcheng@bu.edu

C. Yang*
Department of Electrical and Computer Engineering and Department of Chemistry,
Boston University,
Boston, MA, 02215, United States
Email: cheyang@bu.edu

J. Voillot, A. Facon, C-A Chhuon, J-D Louise, H Moulet*
Axorus SAS,
Loos, 59120, France
Email: helene.moulet@axorus.com

Abstract

Retinal degenerative diseases of photoreceptors are a leading cause of blindness with no effective treatment. Retinal prostheses aim to restore sight by stimulating residual retinal cells. Here, we present a photoacoustic retinal stimulation technology. We designed a polydimethylsiloxane and carbon-based flexible film that converts near-infrared laser pulses into a localized acoustic field with 56-µm lateral resolution, allowing precise stimulation of mechanosensitive retinal cells. This photoacoustic stimulation robustly and locally modulated retinal ganglion cell activity in both wild-type and degenerated *ex vivo* rat retinae. In animals subretinally implanted with a millimeter-sized photoacoustic film , pulsed laser stimulation generated neural modulation along the visual pathway to the superior colliculus, as measured by functional ultrasound imaging. The biosafety of the film was confirmed by the absence of short-term adverse effects , while local thermal increases were measured below 1 °C. These findings demonstrate the potential of photoacoustic stimulation for high-acuity visual restoration in blind patients.

45

Introduction

Retinitis pigmentosa and age-related macular degeneration affect millions of people worldwide[1], resulting in irreversible photoreceptor degeneration and blindness. Currently, there is no effective drug treatment for preventing photoreceptor loss. Retinal prostheses are implantable devices designed to stimulate the residual retinal layers to restore vision[2]. To date, two retinal prosthesis designs, which both primarily use electrostimulation to restore vision, have been approved for commercial implantation[3]. However, both were later removed from the market, facing challenges such as poor spatial resolution and small restored visual field. The more recent photovoltaic-based PRIMA implant, one of the most advanced retinal prostheses currently in clinical trials (NCT04676854), offers a spatial resolution of 100 µm, and a median visual acuity below the threshold for legal blindness[4], and a limited restored visual field of 7°.

Focused ultrasound is a promising noninvasive approach for retinal stimulation[5]. It has been shown to evoke stable responses in the *ex vivo* salamander retina with a 90-µm lateral resolution at 43 MHz[6] and in the *in vivo* blind RCS rat retina with a lateral resolution of around 400 µm with a 4.5-MHz transducer 2D-array[7–9]. However, it still faces safety challenges to meet FDA safety threshold for ophthalmological use[7].

Photoacoustic modulation is an emerging method for high-precision neural stimulation[10,11]. A localized ultrasound field is generated by the photoacoustic agents upon excitation with a pulsed laser, and used to stimulate neurons. High spatial resolution stimulation of single neurons has been demonstrated through a fiber-based photoacoustic emitter[10].

In this study, we investigated photoacoustic retinal stimulation as an alternative strategy for restoring vision. We here provide evidence of its efficacy both *ex vivo* and *in vivo* on healthy and degenerated retinae, as well evidence of the biosafety of the photoacoustic film in short-term implantation.

Results

Fabrication and characterization of the flexible photoacoustic film

The working principle of photoacoustic retinal stimulation is illustrated in Fig. 1a. A 1030-nm pulsed laser is delivered to the back of the eye onto the retina, illuminating the subretinally-implanted flexible photoacoustic (PA) film. Laser absorption by the film produces transient heating, which causes thermal expansion and compression of the material, thereby generating pulsed ultrasound waves. The generated ultrasound waves stimulate the mechanosensitive retinal cells[6,8,12], resulting in a change in retinal ganglion cell activity, which is then transferred to the brain.

The PA film (Fig. 1b) consists of candle soot (CS) as the absorber material, sandwiched between two layers of polydimethylsiloxane (PDMS), which acts as the thermal expansion material. The film has a Young's modulus of 2.12 ± 0.10 MPa to minimize the immune response[13,14] once implanted (Supplementary Fig. S1). Upon excitation with 4.2-ns laser pulses at 7 µJ per pulse, the PDMS/CS/PDMS film emitted ultrasound pulses with a peak-to-peak pressure of 146.2 kPa measured 0.9 mm away (Fig. 1c). At the surface of the film, the conversion efficiency is estimated at 26 kPa.µJ^{-1} based on the distance-dependent pressure profile measured (Supplementary Fig. S2). PA signals were found to have a central frequency of 42.2 MHz and -6 dB bandwidth ranging from 29.6 to 59.9 MHz. This central frequency is an intrinsic property of our film under our experimental conditions, given the fixed laser pulse duration, the Grüneisen parameter of PDMS, and the constant concentration of the CS layer set by the constraints of the flame synthesis process. This central frequency has been demonstrated to activate e*x vivo* salamander retinae with a lower intensity threshold compared to lower acoustic frequencies[15]. These data suggest that the PDMS/CS/PDMS film is a promising photoacoustic converter for retinal stimulation.

The spatial distribution of the ultrasound field generated by the PDMS/CS/PDMS film was further mapped by PA-field microscopy (Fig. 1d, Supplementary Fig. S7). A 50-µm optical fiber was attached to the PA film to ensure a 50-µm-diameter illumination area. The axial pressure profile shows that the maximum acoustic signal is generated at the surface of the film upon illumination (Z = 0 µm) and attenuates to 50% of its peak value at Z = 140 µm (Fig. 1d, right). The lateral width (W) of the acoustic field, quantified by the full width at half maximum, measures W = 56 µm at Z = 0 µm and increases with axial depth to W = 124 µm at Z = 100 µm (Fig. 1e). These results confirm that under a confined illumination, the PA film produces a highly localized, 56-µm lateral ultrasound field comparable to the size of illumination, opening up potential for retinal stimulation with sub-100-µm resolution.

Measured acoustic pressure exhibited a linear relation with the incident laser energy per pulse (Fig. 1f), which indicates that the output pressure can be precisely modulated by adjusting the input laser energy.

The greatest heat increase is assumed to be generated at the level of the PA film, as a consequence of the laser light absorption. Ultrasound absorption could cause an additional increase in temperature, but it is expected to be much lower due to the very low acoustic energy. To ensure that the laser light absorption by the designed PA film is not associated with a substantial and detrimental temperature increase, we measured the temperature at the surface of the PA film. The tested laser conditions were consistent with those employed in the following *ex vivo* retinal stimulation experiments (next section). We observed a maximum temperature rise of 0.52 ± 0.09 °C (Fig. 1g). The baseline change due to cumulative thermal effects was 0.21 °C after 40 s. This value is an order of magnitude below the temperature increase needed for thermal neural modulation[16,17] or tissue overheating. Therefore, the film is unlikely to thermally modulate retinal neuronal activity.

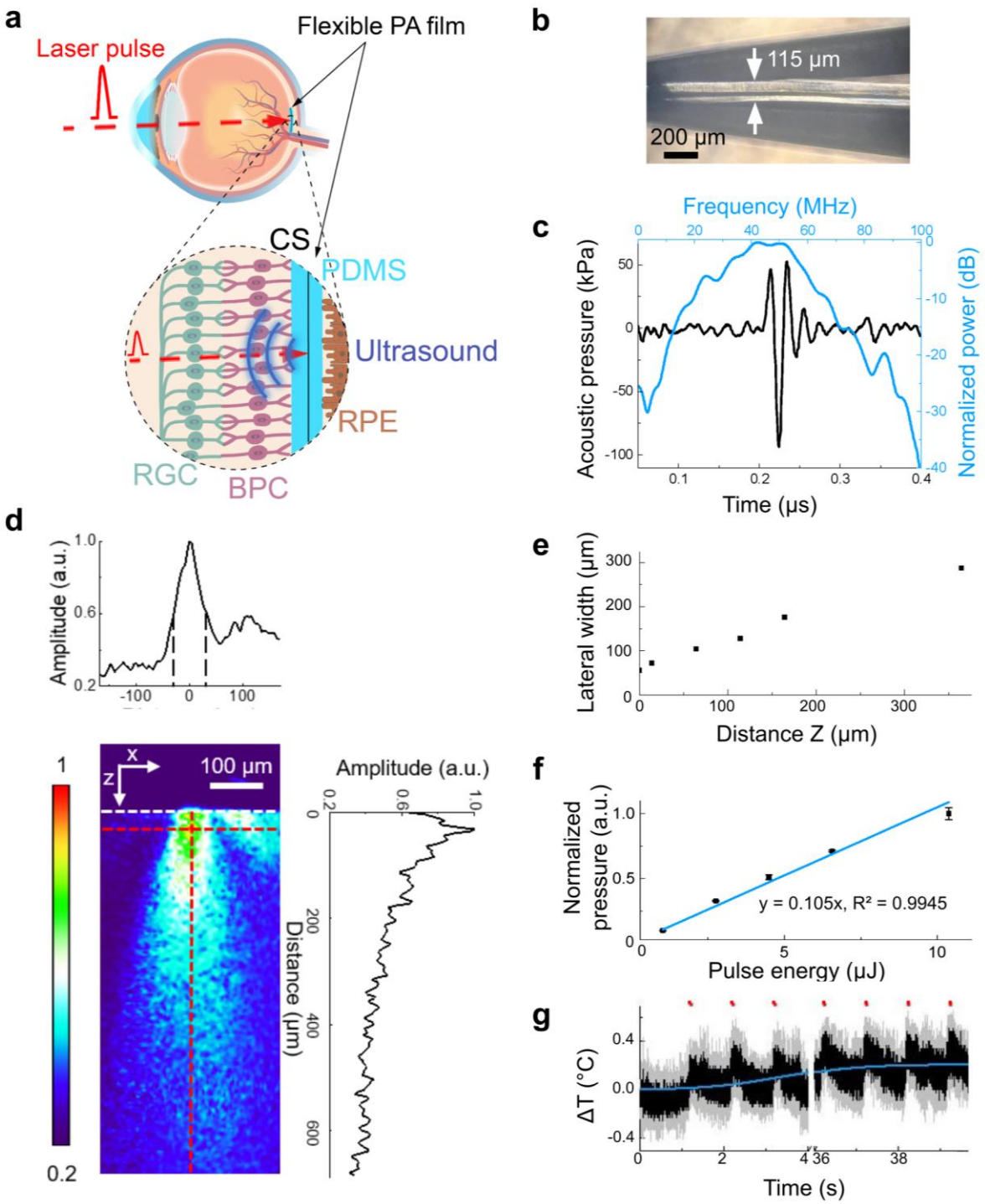

Figure 1. Characterization of the flexible photoacoustic film. (a) Working principle of the flexible photoacoustic (PA) film. Illumination of the PA film (cyan) with a nanosecond pulsed laser (red dashed line) produces an ultrasound emission (blue). CS: candle soot, PDMS: polydimethylsiloxane, RPE: retinal pigment epithelium, RGC: retinal ganglion cells, BPC: bipolar cells. **(b)** A photograph of the PDMS/CS/PDMS film with a three-layer design held by a tweezer. **(c)** Characterization of the PA film in the temporal domain (black) and frequency domain (blue) measured 0.9 mm away from the film

surface. **(d)** Mapping of the ultrasound field generated by the PDMS/CS/PDMS film upon illumination through a 50-µm optical fiber. *Center*: measured distribution of the generated US field. The side lobe on the right of the field is due to the slight tilted angle when the optical fiber was put in contact with the sample film. White dotted line: interface between water and the film. *Top and right*: normalized lateral and axial profiles of the PA field, respectively, measured along the red dashed lines in the center panel. The amplitude of the acoustic signal was normalized to the maximum amplitude measured in the field. **(e)** Full width at half maximum of the lateral profile as a function of the axial position *Z* extracted from (d). **(f)** Peak-to-peak pressure of the PA signal as a function of laser energy per pulse measured from a PDMS/CS/PDMS film by a hydrophone. The pressure was normalized to the maximum pressure in all measurements. N = 3 for each data point. Blue line: linear fitting: $y = 0.105x$, $R^2 = 0.9945$. **(g)** Temperature increase at the surface of the PA film following illumination with a 200-µm laser spot. N = 3 for each data point, mean (black line) ± SD (gray shade). Red dots: laser on. Laser parameters: energy of 10 µJ per pulse, repetition rate of 3 kHz (laser power density $P = 0.95$ W/mm^2), and burst duration 50 ms, delivered every 1 s over 40 s. The baseline change due to cumulative thermal effect was determined by logistic curve fitting of the data (blue line).

135

136 **Photoacoustic modulation of the *ex vivo* retina**

137 To evaluate retinal responses following photoacoustic stimulation, we recorded the activity of retinal
138 ganglion cells (RGCs) from *ex vivo* retinae of wild-type Long-Evans (LE) rats on a multi-electrode array
139 (n = 4 rats). The PDMS/CS/PDMS film was placed on the *ex vivo* retina against the photoreceptor layer.
140 It was photoactivated by a 1030-nm pulsed laser delivered through a 200-µm optical fiber (Fig. 2a),
141 which was successively moved at different positions between stimulations. We applied 4.2-ns laser
142 pulses at a repetition rate of 1.9 kHz (every 520 ns) for a burst duration of d_b = 10 ms, with a pulse
143 energy of 10 µJ (Fig. 2b, top; power density P = 0.27 $W.mm^{-2}$), yielding an estimated peak-to-peak
144 ultrasound pressure of 0.12 MPa.

145 Photoacoustic stimulation evoked robust RGC responses in healthy LE retinae (Fig. 2b, 2c, top two
146 panels). Individual RGCs were considered responsive or modulated if their firing rate significantly
147 increased (excited response) or decreased (inhibited response) relative to baseline (Fig. 2c, 2e). 100
148 LE RGCs (78%) exhibited an alteration in activity upon PA stimulation (Fig. 2e) out of the 129
149 spontaneously active RGCs on the electrodes contained in a 300-µm-radius area centered on the laser
150 spot. Responsive RGC activity was mainly increased (92% of responding RGCs, Fig. 2d, left). RGCs with
151 an increased activity had a mean response firing rate of 66 ± 3.7 Hz (Fig. 2f), and had a mean response
152 latency of 51 ± 34.2 ms (Fig. 2g). The response latency was inversely correlated with the firing rate
153 (Fig. 2h).

154 To investigate the potential of such photoacoustic stimulation for restoring vision, we then stimulated
155 *ex vivo* retinae from blind P23H rats (n = 4 rats). Similarly to LE retinae, though with a lower fraction,
156 89 out of 229 P23H RGCs (39%) exhibited robust responses to photoacoustic stimulation (Fig. 2c-e),
157 predominantly with increased activity (93% of responding RGCs). Compared to LE RGCs, P23H RGC
158 firing rate was significantly lower following stimulation (29 ± 2.88 Hz, Fig. 2f) and response latency was
159 significantly increased (89 ± 65 ms, Fig. 2g). Only 36% of P23H RGCs had response latencies below 45
160 ms[12], which was significantly fewer than LE cells (39%, Fig. 2g). These results on the P23H rat retina
161 demonstrate the *ex vivo* efficacy of photoacoustic stimulation in modulating retinal ganglion cells
162 activity in degenerated retinae.

163 To rule out the possibility that the healthy LE retina was responding to the pulsed infrared laser
164 light[18,19], we applied direct laser pulses to the LE rat retina. Using identical laser conditions to those
165 applied on the film, only 3.6 ± 0.9% of recorded RGCs showed a modified activity following directfilm
166 stimulation, compared to 77 ± 20% of recorded RGCs following on-film photoacoustic stimulation (Fig.
167 2i). These results were further confirmed in *in vivo* LE rats (see below). Furthermore, we found that
168 the PA film absorbs more than 99% of the infrared laser energy (Supplementary Fig. S3). These results

confirmed that the infrared laser light filtered out through the implant was not sufficient to directly activate the retinal circuit in the healthy LE retina.

171

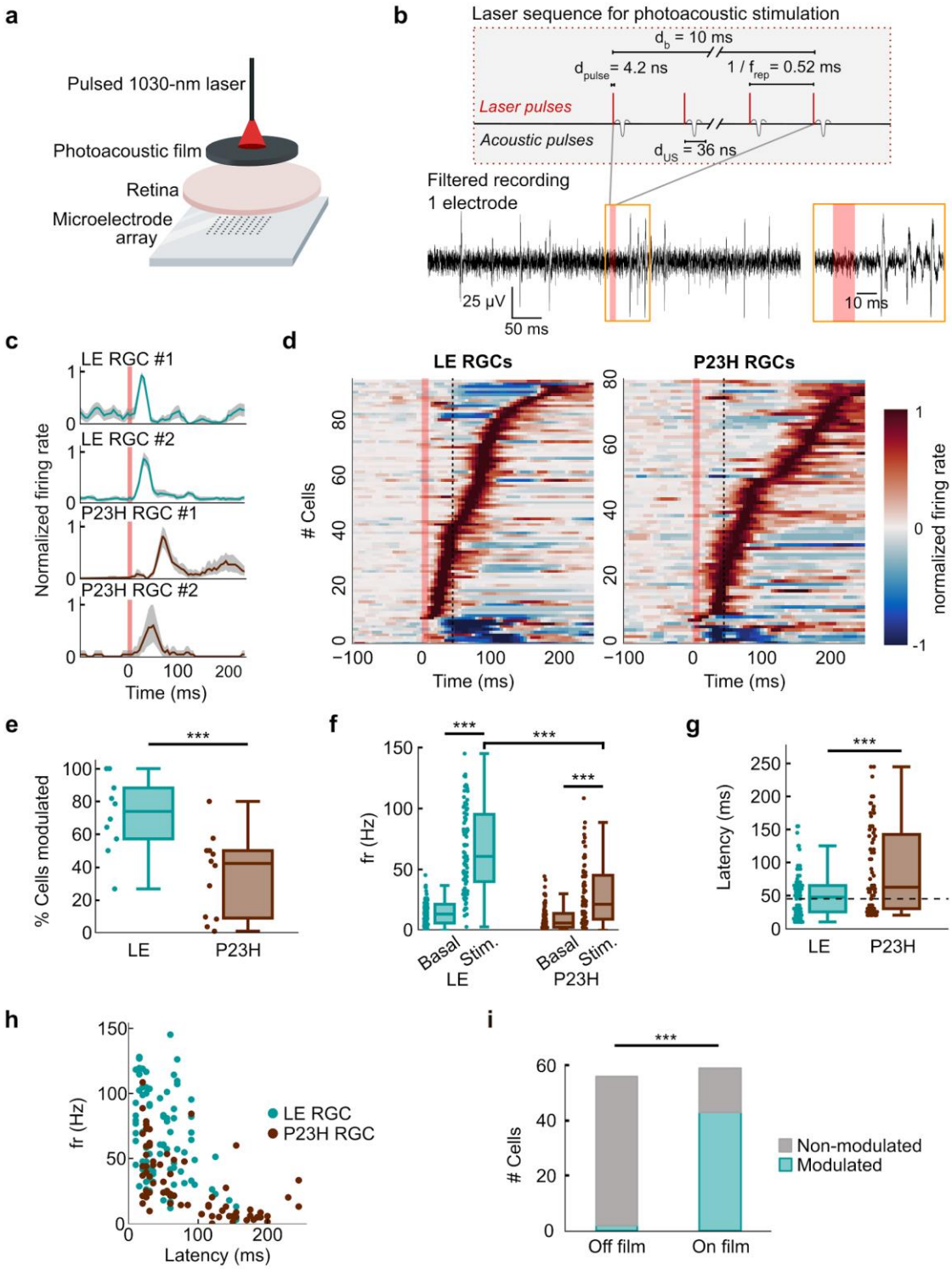

Figure 2. Photoacoustic modulation of *ex vivo* wild type and degenerated retinae. (a) The *ex vivo* retina was placed on a multi-electrode array (MEA) with the photoacoustic film against the photoreceptor layer. **(b)** *Top*: schematic of the laser sequence for photoacoustic stimulation. Laser pulses, with an energy of E_p = 10 µJ per pulse and duration d_{pulse} = 4.2 ns, were delivered at a repetition frequency f_{rep} = 1.9 kHz during a single burst of duration d_b = 10 ms. Each laser pulse is converted by

178 the PA film into an acoustic wave with a duration d_{US} = 36 ns. *Bottom*: Example high-pass filtered MEA
179 recording from a single electrode displaying elicited spikes following a photoacoustic stimulation. Red
180 shaded area: laser on. Inset: zoom in of action potentials following stimulation. **(c)** Examples of Long
181 Evans (LE) and P23H RGC responses to photoacoustic stimulation. Cyan (LE) and brown (P23H) lines:
182 mean firing rate. Gray shaded areas: 99% bootstrapped CI from 1000 samples. Red shaded area: PA
183 stimulation. **(d)** Heatmaps of normalized firing rates for responsive LE RGCs (left, n = 100) and P23H
184 RGCs (right, n = 88). Red shaded area: PA stimulation. Dashed black line: 45-ms cutoff for slow and
185 fast latency responses. Cells with excited responses display an increase in firing rate after
186 photoacoustic stimulation (red), and cells with inhibited responses display a decrease in firing rate
187 (blue). **(e)** Percentage of cells modulated by photoacoustic stimulation per stimulation site. LE: 74% (4
188 rats, n = 10 stimulation sites), P23H: 39 %, (4 rats, n = 12 stimulation sites). *** $p < 0.001$, Mann
189 Whitney U test. **(f)** Firing rates of LE and P23H RGCs during baseline (basal) and following stimulation
190 (stim). Mean firing rates: LE: fr_{basal} = 14 ± 1.0 Hz, fr_{stim} = 66 ± 3.7 Hz (n = 82 RGCs within stimulation
191 range, $p < 0.001$, Wilcoxon signed-rank); P23H: fr_{basal} = 10 ± 1.2 Hz, fr_{stim} = 29 ± 2.88 Hz (n = 72 RGCs
192 within stimulation range, $p < 0.001$, Wilcoxon signed-rank). **(g)** Latencies of RGC responses for LE (51
193 ± 34.2 ms, mean ± standard deviation) and P23H (89 ± 65 ms, $p < 0.001$ Wilcoxon rank-sum)). Dashed
194 black line: 45-ms cutoff for slow- and fast-latency responses. **(h)** Firing rate of modulated RGCs as a
195 function of response latency. Firing rate and response latency of excited RGCs were correlated for LE
196 ($r = -0.40$, $p < 0.001$, Pearson correlation) and P23H ($r = -0.59$, $p < 0.001$, Pearson correlation) RGCs. **(i)**
197 Off-film laser light stimulation. Percentage of LE RGCs modulated by direct laser stimulation on the
198 retina ("off film") compared to photoacoustic stimulation ("on film"). Laser parameters: E_p = 10 µJ per
199 pulse, f_{rep} = 3.5 kHz, d_b = 10 ms. Off film: 3.6% ± 0.9% (n = 56 cells, 2 retinae), on film: 77% ± 20% (n =
200 59 cells, 3 retinae). Statistics: * $p < 0.05$, *** $p < 0.001$, Mann-Whitney U test.

201

202 **Mechanistic exploration of retinal mechanosensitivity**

203 It is currently unclear which layers in the retina contribute to the mechanosensitivity of the retina. We
204 first observed an increase in response latency when photoreceptors have degenerated in P23H rat
205 retinae, compared to LE retinae (Fig. 2g). To assess if photoreceptors initiate the short-latency US
206 response, we bath-applied the group III mGluR agonist L-AP4 to LE retinae (Fig. 3a-c), which blocks the
207 synaptic transmission between photoreceptors and ON bipolar cells[43]. We subsequently applied the
208 kainate agonist ACET, which blocks most of the remaining glutamatergic synapses.

209 Before application of the blockers, a large fraction of recorded RGCs was responsive to the PA
210 stimulation (58%, Fig. 3a, No blocker) with strong response firing rates (103 ± 2 Hz, Fig. 3a, No blocker).
211 Following L-AP4 application, fewer RGCs were responsive to PA stimulation (19%, Fig. 3b, L-AP4), and
212 their firing rates following stimulation were highly decreased (37 ± 6 Hz, Fig. 3b, L-AP4). Moreover, L-
213 AP4 predominantly suppressed short-latency responses (<45 ms, 7% of recorded cells, Fig. 3c, L-AP4).
214 These short-latency responses were recovered after the washout of the L-AP4 (Fig. 3c, baseline and
215 washout): The L-AP4 condition mimics what was observed with recordings of P23H rat retinae with
216 degenerated photoreceptors ($p = 0.993$, 2-sided Mann Whitney-U). These results further support that
217 photoreceptors generate most of the short-latency RGC responses to ultrasound.

218 Addition of ACET to L-AP4 further suppressed RGC responses to PA stimulation (L-AP4 + ACET:
219 8 %, L-AP4: 19%, control with no blockers; 55%, Fig. 3b). This additional effect of ACET indicated that
220 cells in the inner retina, upstream of RGCs, are also contributing to the production of the US-mediated
221 RGC activation. These pharmacological data indicate that part of the RGC responses to PA stimulation
222 rely on upstream singaling pathways. Taken together, these results demonstrate the important
223 contribution of photoreceptors in the short-latency response to ultrasound stimulation, as shown by
224 previous studies[6,18], and reliance of PA-mediated stimulation on upstream signaling.

225 Finally, to isolate the contribution of RGCs in PA-induced responses in the P23H model, we
226 bath-applied glutamatergic blockers (rs)-CPP and CNQX to P23H retinae (Fig. 3d, e). PA-induced
227 responses were nearly completely abolished, but not recovered following the washout of the blockers
228 (basal: 24 %, CPP+CNQX: 8 %, washout: 8 %, Fig. 3e). The lack of recovery during washout could be
229 attributed to the difficulty of removing CPP and CNQX. These results suggest that the main
230 mechanosensitive cells are upstream of RGCs, consistent with previous studies[6,12,18,19], and that
231 glutamate neurotransmission is required to transfer the mechanosensitive signal to the RGCs.

232

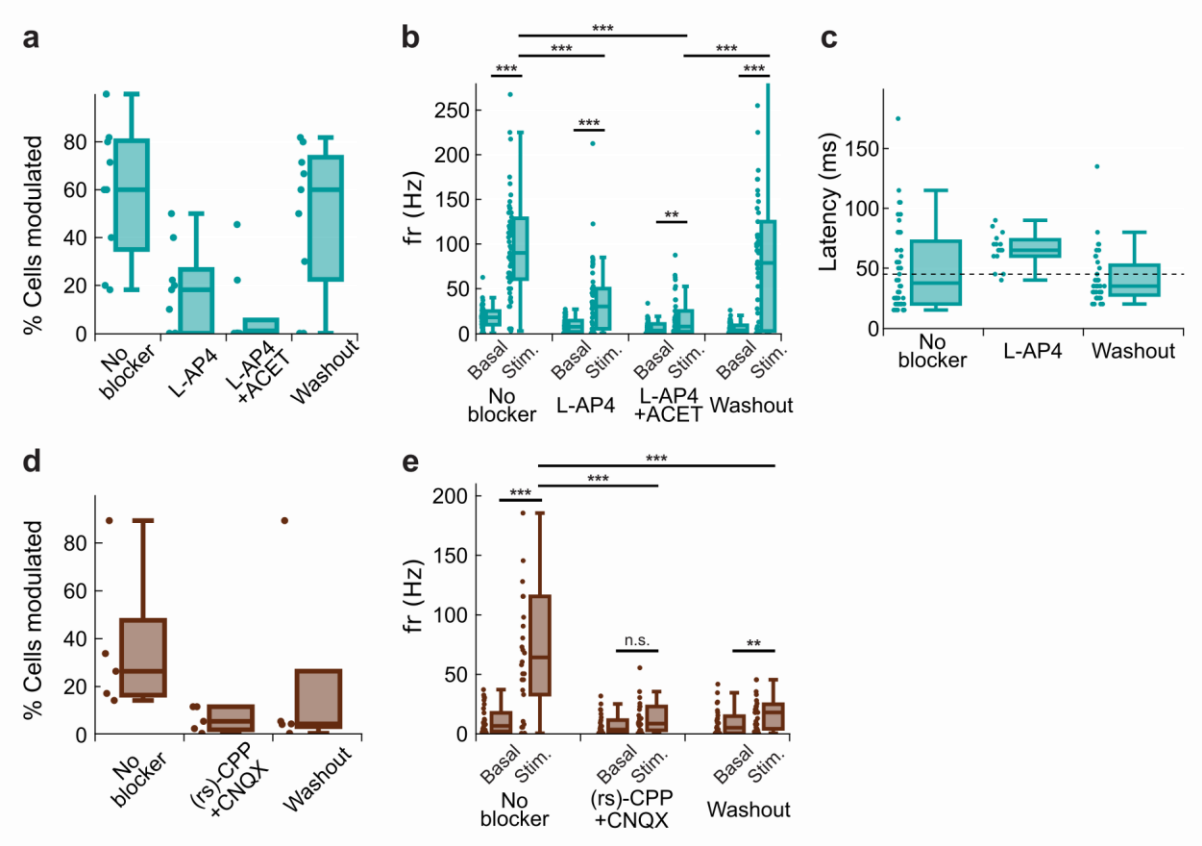

Figure 3. Photoacoustic responses under pharmacological blocking. (a) Percentage of cells modulated by photoacoustic stimulation per stimulation site before and after L-AP4 application. *No blocker*: 49%; *L-AP4*: 16%; *L-AP4 + ACET*: 7%; *washout:* 40% (2 retinae, n = 9 stimulation sites). **(b)** Group III mGluR agonist L-AP4 decreased RGC spontaneous firing rate and firing rate during PA-elicited responses in LE retinae. The population firing rate of RGCs (n = 41 cells, 2 retinae) is compared between baseline (Basal) and stimulation (Stim.), before blocker application (No blocker), following blocker application (L-AP4) and after washout (Washout) with Ringer medium. Firing rates per condition, *no blockers*: fr_{basal} = 18 ± 2Hz, fr_{stim} = 103 ± 9 Hz ($p < 0.001$); *L-AP4*: fr_{basal} = 9 ± 1 Hz, fr_{stim} = 37 ± 6 Hz ($p < 0.001$); *L-AP4+ACET*: fr_{basal} = 6 ± 1 Hz, fr_{stim} = 16 ± 3 Hz ($p = 0.024$), *washout*: fr_{basal} = 7 ± 1 Hz, fr_{stim} = 86 ± 13 Hz ($p < 0.001$). Comparison of the population stimulation firing rate fr_{stim} after blocker application and fr_{stim} before application ($p < 0.001$), and fr_{stim} after washout ($p < 0.001$). **(c)** L-AP4 increases response latency in LE retinae. Response latency per condition, *no blockers*: 49 ± 5 ms; *L-AP4*: 65 ± 4 ms; *washout*: 42 ± 3 ms. Comparison of the response latency before blocker application and after ($p < 0.001$, Wilcoxon signed-rank), and after washout (Friedmanchi square, $p = 0.4$). Due to absence of responses during application of L-AP4+ACET blockers, no latencies are reported for this group. Dashed black line: 45-ms cutoff for slow- and fast-latency responses. **(d)** Percentage of cells modulated by photoacoustic stimulation per stimulation site before and after (rs)-CPP and CNQX application in P23H retinae. *No blocker*: 42 %; *(rs)-CPP + CNQX*: 5 %; *washout:* 8 % (2 retinae, n = 5 stimulation sites). **(e)**

252 Glutamate blockers (rs)-CPP and CNQX abolished RGC responses to PA stimulation in P23H retinae.
253 The population firing rate of RGCs (n = 25 cells, 2 retinae) is compared between baseline (basal) and
254 stimulation (stim), before blocker application (no blocker), following blocker application ((rs)-
255 CPP+CNQX) and after washout (washout) with Ringer medium. Firing rates per condition, *no blockers*:
256 fr_{basal} = 11 ± 2 Hz, fr_{stim} = 100 ± 23 Hz ($p < 0.001$); (rs)-*CPP+CNQX*: fr_{basal} = 7 ± 2 Hz, fr_{Stim} = 23 ± 10 Hz (p
257 =0.141); *washout*: fr_{basal} = 8 ± 2 Hz, fr_{stim} = 24 ± 9 Hz ($p = 0.016$). Comparison of the population
258 stimulation firing rate fr_{stim} after blocker application and fr_{stim} before application ($p < 0.001$, Wilcoxon
259 signed-rank), and fr_{stim} after washout ($p < 0.001$, Wilcoxon signed-rank). For each panel, groups are
260 tested for significant differences using Friedman chi square, with post-hoc Wilcoxon signed-rank. p-
261 values are holm-corrected (***: $p<0.001$, **: $p<0.05$).

262

263 **Dependence of RGC response on laser conditions**

264 We further investigated RGC responses to photoacoustic stimulation using different laser repetition
265 rates (10 µJ per pulse, f_{rep1} = 1.9 kHz with P_1 = 0.27 mW.mm^{-2} and f_{rep2} = 3.5 kHz with P_2 = 0.52 mW.mm^{-}
266 ^{2}) and burst durations (d_b = 5 - 30 ms). In LE retinae, the firing rates of cells with excited responses
267 increased with burst durations up to d_b = 25 ms for f_{rep1}, while at f_{rep2} they plateaued up to d_b = 15 ms
268 and decreased with longer burst durations (Fig. 4a-b, left). P23H RGCs with excited responses also
269 showed an increase in firing rate with longer burst durations for f_{rep1} (Fig. 4a-b, right), while firing rate
270 increased for burst durations up to d_b = 20 ms then decreased with longer burst durations for f_{rep2} (Fig.
271 4b, right). LE RGC firing rates were significantly higher than those for P23H RGCs, up to 2.8-fold during
272 d_b = 25 ms and up to 4.7-fold during d_b = 20 ms with f_{rep1} and f_{rep2}, respectively (Fig. 4b). These results
273 suggest that the degenerated retina requires stronger photoacoustic stimulation, consistent with
274 previous findings concluding on a higher acoustic stimulation threshold in degenerated retinae
275 compared to wild-type retinae[8]. LE RGC response latencies did not increase with burst duration or
276 repetition rate (Fig. 4c), nor did P23H RGC latencies.

277

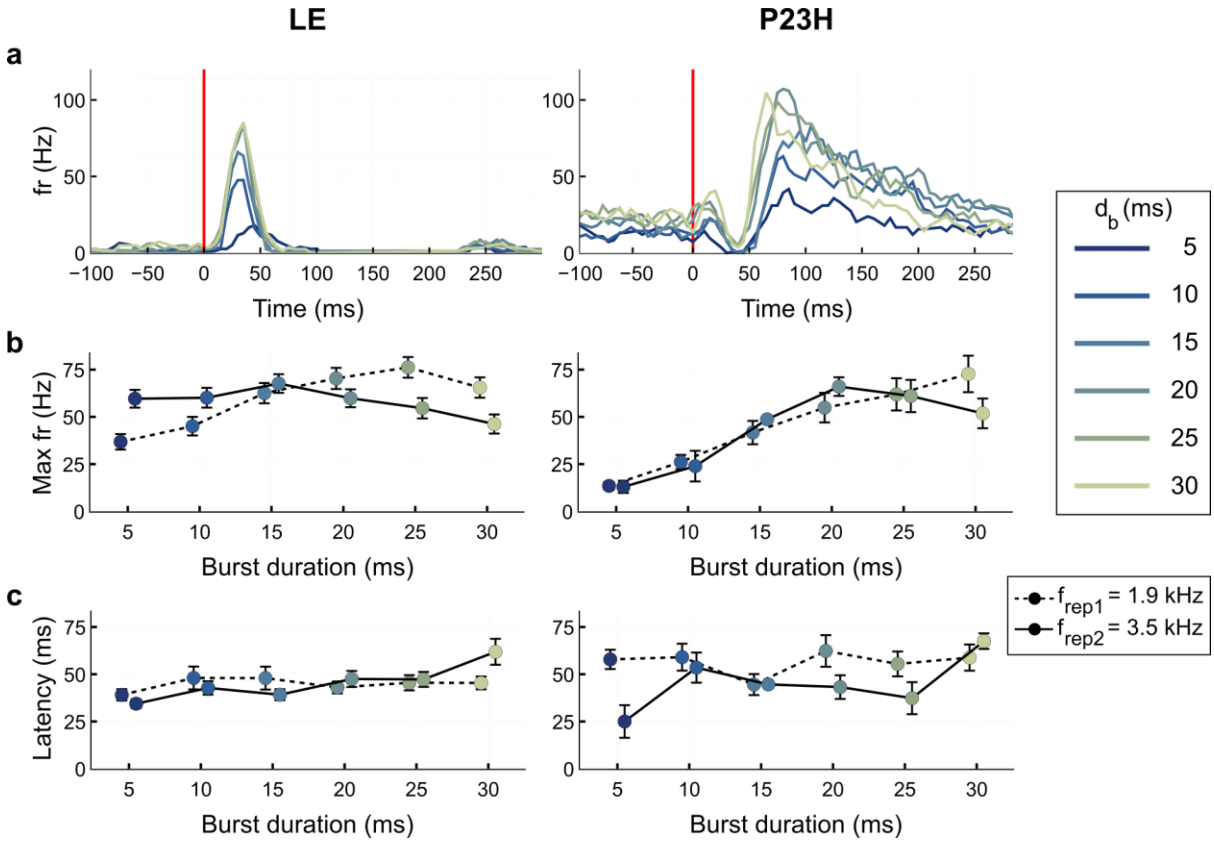

Figure 4. RGC responses under different laser burst durations and laser repetition rates. (a) Example LE (left) and P23H (right) cells showing increased maximum firing rate (fr) with increased burst duration (recorded at f_{rep1} = 1.9 kHz). Lighter colors indicate longer burst durations (d_b= 5-30 ms). Vertical red lines: laser onset. **(b)** Maximum firing rate as a function of burst duration for LE and P23H RGCs during stimulation with repetition frequencies f_{rep1} = 1.9 kHz (dashed line) and f_{rep2} = 3.5 kHz (solid line). Data are plotted as mean + SE. In LE RGCs (left panel), the firing rate was positively correlated with burst duration for f_{rep1} ($r = 0.91$, $p = 0.01$, Pearson R). In P23H RGCs (right panel), the firing rate was positively correlated during both f_{rep1} ($r = 0.996$, $p < 0.001$) and f_{rep2} ($r = 0.811$, $p = 0.05$). With f_{rep1}, for d_b = 5 ms and 20 ms, the maximum firing rate of LE RGCs was 2.8- and 1.3-fold higher, respectively, than for P23H RGCs ($p < 0.001$ for all conditions, Mann-Whitney U-test). With f_{rep2}, for d_b = 5 ms, the maximum firing rate of LE RGCs is 4.7-fold higher than for P23H RGCs ($p < 0.001$, Mann-Whitney U-test). **(c)** Response latency as a function of burst duration for LE and P23H RGCs showed no significant correlation (LE: $p = 0.70$ and $p = 0.19$ for f_{rep1} and f_{rep2}, respectively; P23H: $p = 0.79$ and $p=0.61$, Pearson R). In both (b) and (c), dashed lines: f_{rep1} = 1.9 kHz (P_1 = 0.27 W.mm^{-2}). Solid lines: f_{rep2} = 3.5 kHz (P_2 = 0.52 W.mm^{-2}). Dataset for (b) and (c): for LE, n = 244 cells, recorded from 4 retinae. For P23H, n = 104 cells, recorded from 4 retinae.

295 **Spatial resolution of *ex vivo* photoacoustic retinal stimulation**

296 To investigate the spatial resolution of the photoacoustic retinal stimulation, we sequentially targeted
297 multiple positions on the film by moving the laser-delivering 200-µm fiber at different sites above the
298 photoacoustic film and mapped the responsive retinal cells (Fig. 5a). The laser repetition rate was set
299 at f_{rep1} = 1.9 kHz for LE retinae (n = 11 sites) and f_{rep2} = 3.5 kHz for P23H retinae (n = 6 sites), to account
300 for the higher modulation threshold previously described for P23H retinae.

301 To assess the spatial distribution of PA-modulated RGCs with excited responses, we mapped the
302 maximum RGC firing rate relative to the stimulation site (Fig. 5b). For both LE and P23H RGCs, the
303 maximum firing rates were located within an area slightly larger than the laser spot (< 400 µm from
304 center), and were negatively correlated with the distance from the laser spot (Fig. 5c). Furthermore,
305 the percentage of responsive RGCs decreased when increasing the distance from the center of the
306 laser spot (Fig. 5d). 73% of LE RGCs and 70% of P23H RGCs were modulated within a 100-µm distance,
307 compared to 14% of LE RGCs and 6% of P23H RGCs at a 400-µm distance. These results indicate that
308 stimulation with the PA film induces a localized response and demonstrate the potential for a high
309 spatial resolution in photoacoustic stimulation.

310

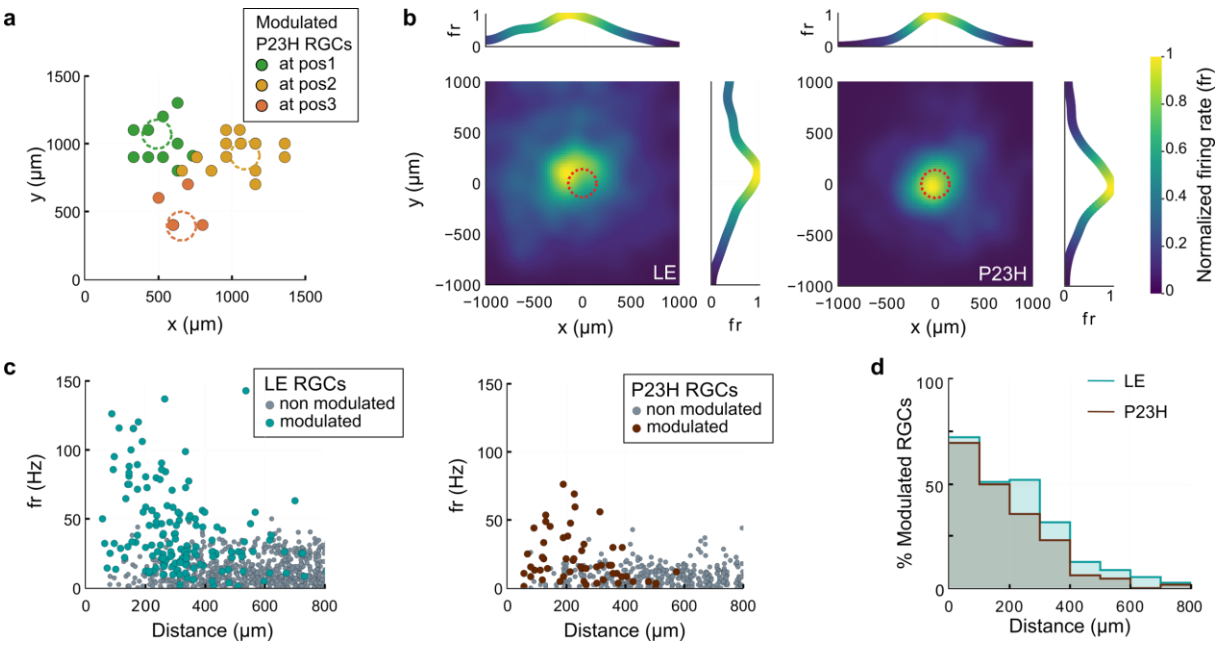

Figure 5. Spatial distribution of RGC modulation upon photoacoustic stimulation. (a) Different populations of RGCs were modulated by moving the laser fiber at different sites on the film. Example of a P23H retina stimulated at three sites; modulated cells at each stimulation site are grouped by color. The 300-µm-diameter laser spots are marked by dashed circles. **(b)** RGC firing rate of modulated cells normalized to maximum firing rate, mapped relative to the stimulation site for LE (left, 4 retinae, 11 stimulation sites) and P23H (right, 4 retinae, 6 stimulation sites). RGC maximum firing rates were averaged across all recorded cells at the same XY coordinates relative to the center of the laser spot (LE: n = 576 and P23H: n = 157 RGCs). Data were smoothed using convolution with a 100-µm gaussian kernel. Dashed circle: 300-µm-diameter laser spot. The shift between the maximum firing rate and the laser spot may be due to uncertainty in the laser spot coordinates, due to the 100-µm pitch of the MEA used for indirect measurement of the exact laser position. **(c)** Maximum firing rate for individual cells as a function of distance from the laser for LE (left) and P23H (right) RGCs. The response firing rate is negatively correlated with distance (LE: $r = -0.310$, $p < 0.001$. P23H: $r = -0.268$, $p < 0.05$, Pearson R). Each circle represents an individual cell. Cyan and brown: LE and P23H RGCs modulated by photoacoustic stimulation, respectively. Gray: non-modulated cells. **(d)** Percentage of RGCs modulated as a function of distance from the laser spot. Cyan: LE cells. Brown: P23H cells. Datasets for (c) and (d) are the same as for (b).

329

330 ***In vivo* safety of the photoacoustic implants**

331 To test the feasibility of photoacoustic stimulation and the biosafety of the film *in vivo*, we chronically
332 implanted 1-mm-diameter PA films in the subretinal space of LE and P23H rats. To investigate whether
333 there is a risk of increased degeneration of inner retinal layers with the 115-µm-thick PDMS/CS/PDMS
334 film, we also prepared and studied a thinner PDMS-CNT film. The PDMS/CS/PDMS film, used in the
335 previous *ex vivo* experiments, was optimized for high photoacoustic conversion efficiency and easy
336 handling. A thinner 40-µm-thick uniformly mixed PDMS-CNT film (characterized in Supplementary Fig.
337 S4) was designed to approach the 30-µm thickness of the clinically tested PRIMA photovoltaic implant,
338 which has shown no long-term adverse effects aside from minor retinal thinning in patients[4]. Both
339 types of films were treated with oxygen plasma to make them hydrophilic, in order to improve cell
340 adhesion and thus minimize the risks of implant displacement.

341 After implantation, eye fundus imaging confirmed the correct positioning of the implant near the optic
342 nerve and the overall integrity of the retina (Fig. 6a-b). No complications, such as retinal tearing after
343 implantation or major inflammation after 7 days post-implantation (dpi), were observed on the OCT
344 images and eye fundus exams. Although the presence of glial cells between the implant and the retina
345 is expected, stimulation efficacy should not be affected, as acoustic attenuation is below 10 $dB.mm^{-1}$
346 [20].

347 On OCT, the average retinal thickness was 174.0 ± 2.3 µm for LE rats (n = 13) and 72.3 ± 2.3 µm for
348 degenerated P23H rats (n = 8). At the PDMS/CS/PDMS implant position, LE retinal thickness decreased
349 to 123.2 ± 2.9 µm at 15 dpi, 121.5 ± 4.2 µm at 30 dpi, and 107.3 ± 2.0 µm at 90 dpi (Fig. 6c). In LE rats
350 implanted with the PDMS-CNT implant, similar values of 113.0 ± 4.8 µm at 15 dpi and 105.8 µm at 30
351 dpi were measured (Fig. 6c). The decrease in the retinal thickness above the implant in LE rats was
352 likely due to photoreceptor degeneration (Fig. 6a, right), caused by the physical separation of
353 photoreceptors from the retinal pigment epithelium, as previously reported with other prostheses[21,22].
354 In implanted P23H rats, retinal thickness above the implant remained stable and comparable to the
355 neighboring area for up to four months for both PDMS/CS/PDMS and PDMS-CNT implants (Fig. 6d).

356 Finally, we performed immunohistochemistry assays on LE (n = 3) and P23H (n = 4) rats. We confirmed
357 the absence of rods and cones at the level of the implant in LE rats (Fig. 6e, *i*). We also observed the
358 presence of activated microglia at the implantation site in both LE (Fig. 6e, *ii*) and P23H rats (Fig. 6f,
359 *ii*), and of activated Müller glia only in LE rats (Fig 6e, *iii*; P23H: Fig 6f, *iv*). No inflammation was
360 observed in the zone surrounding the implant (Fig 6e-f, *iv*), except for a highly inflamed zone (Fig. 6e,
361 *iv*, bottom right corner), which corresponded to the insertion track of the implant during surgery.
362 Future studies will need to refine the implantation surgery of the PA implant to minimize inflammation

363 caused by the insertion of the implant. Surface modification of the PDMS may also be explored to
364 minimize inflammation at the level of the implant, in particular to reduce potential fibrosis.

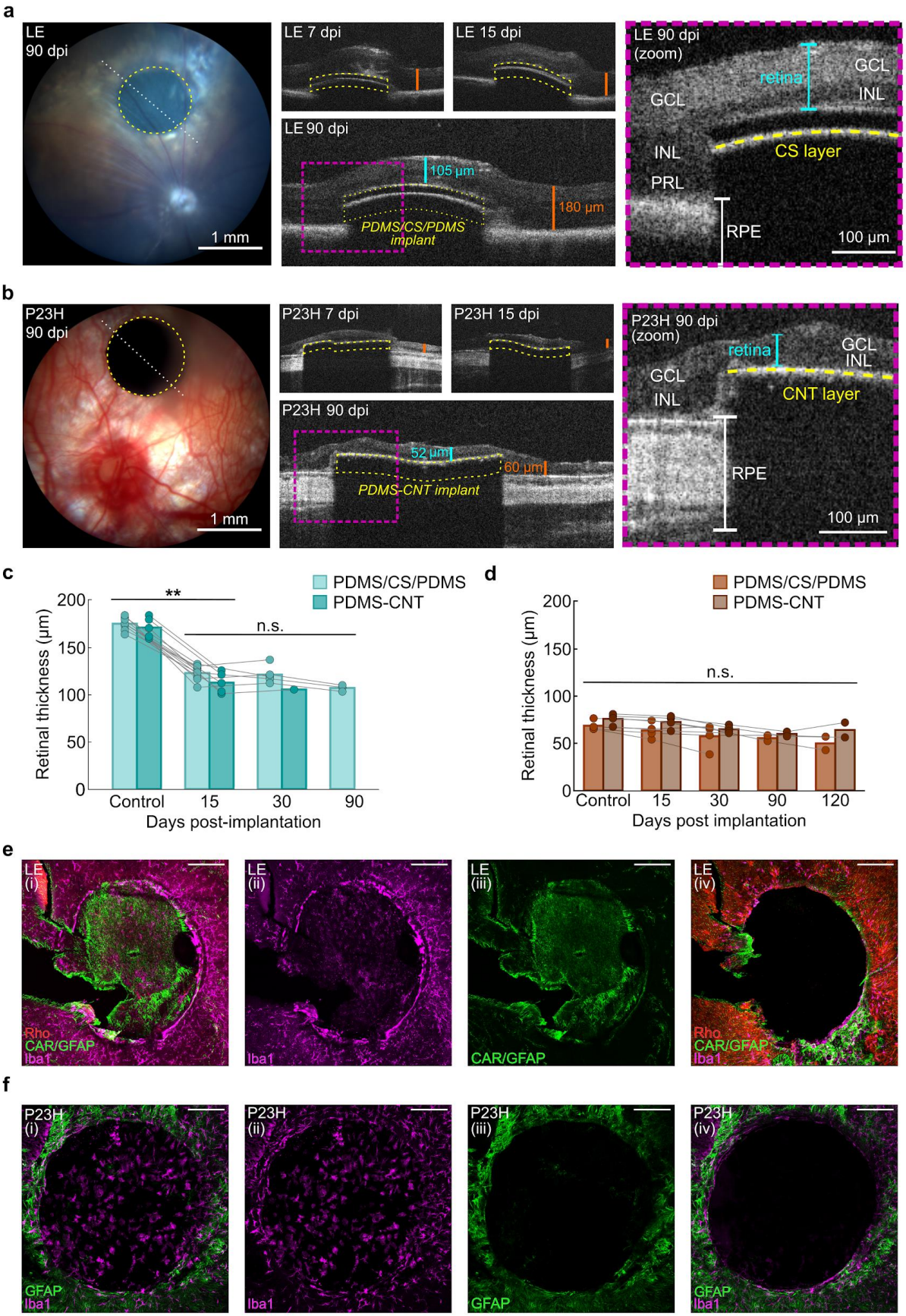

Figure 6. *In vivo* photoacoustic implant biocompatibility. (a) Eye fundus (left) and OCT images (middle

367 and right) of an LE rat retina with a subretinal PDMS/CS/PDMS implant (yellow dotted line) at 7, 15,
368 and 90 days post-implantation (dpi). OCT images were taken along the white dotted line shown in the
369 left panel. In the zoomed-in OCT images, GCL: retinal ganglion cell layer, INL: inner nuclear layer, PRL:
370 photoreceptor layer. RPE: retinal pigmented epithelium. The PR layer has degenerated above the
371 implant. Right inset: zoom on the OCT image at 90 dpi. **(b)** Same as (a) but for a P23H rat. **(c)** Mean LE
372 retinal thickness above PDMS/CS/PDMS (light cyan) and PDMS-CNT (dark cyan) implants over time.
373 Control: mean retinal thickness next to the implant at 15 dpi. Thickness at 15 dpi and later is
374 significantly lower than control thickness (**$p < 0.01$, Wilcoxon Signed-Rank test). At 15 dpi, the
375 thickness above PDMS/CS/PDMS implants is not statistically different from the thickness above PDMS-
376 CNT implants ($p = 0.16$, Mann-Whitney U test). Between 15 dpi and 90 dpi, the decrease in thickness
377 above PDMS/CS/PDMS implant (123.2 ± 2.9 µm to 107.3 ± 2.0 µm) is not significant ($p = 0.25$, Wilcoxon
378 Signed-Rank test). **(d)** Same as (c) for P23H rats. The difference of retinal thickness above both
379 implants is not statistically significant ($p = 0.16$ at 15 dpi and 0.32 at 30 dpi, Mann-Whitney U-test).
380 Retinal thickness is stable up to 120 dpi for both PDMS-CNT ($p = 0.18$, one-way ANOVA) and
381 PDMS/CS/PDMS implants ($p = 0.51$). **(e)** Immunolabeling of an implanted LE retina, labeling rods (Rho,
382 red, *i, iv*), cones (CAR, green, *i, iii*), microglia (Iba1, magenta, *i*, *ii*, *iv*), and Müller cells (GFAP, green, *i,*
383 *iii*). *i - iii*: implanted zone. *iv:* zone surrounding the implant. **(f)** Same as (e) for P23H, with microglia
384 (Iba1, magenta, *i*, *ii*, *iv*) and Müller cells (GFAP, green, *i, iii*). Scale bar for (e) and (f) is 200 µm.

385

386 **Photoacoustic retinal stimulation *in vivo***

387 We then examined *in vivo* photoacoustic stimulation of the degenerated retina using subretinal
388 PDMS/CS/PDMS and PDMS-CNT implants in LE rats. As mentioned in the previous section (Fig. 6a, c),
389 the local detachment of the retina from the retinal pigment epithelium (RPE) caused by the implant
390 induces local degeneration of photoreceptors in LE rats at the location of the implant, creating a
391 localized model of retinal degeneration at the photoacoustic stimulation site (Fig. 6e, f). Activation of
392 the visual pathway was assessed in the contralateral Superior Colliculus (cSC) using functional
393 ultrasound imaging (fUSI), which measures relative changes in cerebral blood volume (rCBV) triggered
394 by neuronal excitation (Fig. 7a). We chose to record the cSC instead of the primary visual cortex (V1)
395 since anesthesia adversely affects the capability of fUSI to detect activation in V1[30,31]. A cranial window
396 was generated just prior to the experiment, preventing a long-term follow-up on the colliculus activity.
397 To verify the coordinates of the cSC, we measured its natural visual activation using control full-field
398 white light stimulation of the implanted eye (P = 0.02 $mW.mm^{-2}$). This generated a large rCBV response
399 area in the cSC (Fig. 7c, i), which was used as a reference area in further analyses (Fig. 7f). We
400 measured a large increase in the amplitude of the rCBV, averaged on a 29-by-29-pixel (29 pixels = 302
401 ± 10 µm) square region of interest (ROI; Fig. 7f, light gray), which was centered on the maximum
402 responses in the cSC. The same ROI was subsequently used to compute the averaged rCBV for all of
403 the stimulation conditions (Fig. 7f). To better define the expected size of the activated area for PA
404 stimulation, we focused a 400-µm-diameter spot of 595-nm laser light (P = 0.21 $mW.mm^{-2}$) onto the
405 healthy retina next to the implant (Fig. 7b, iii). It similarly triggered an increase in rCBV in the cSC (Fig.
406 7c, ii), with an activated area representing 32 ± 11 % (n = 6) of the area activated by the full-field white
407 light (Fig. 7f). In the same 29-by-29-pixel ROI, the rCBV amplitude and response kinetics were similar
408 to those generated by the full-field white light stimulation (Fig. 7g, orange).

409 We then proceeded with photoacoustic stimulation on the implants (Fig. 7b, ii; Fig. 7d, top). The 1030-
410 nm laser delivered eight 125-ms bursts during 2 s, repeated every 15 s, for a total of 15 stimulations
411 per recording (Fig. 7d). Laser power densities were P = 0.29 ± 0.06 $W.mm^{-2}$ (mean ± SD) for
412 PDMS/CS/PDMS implants and P = 0.39 ± 0.12 $W.mm^{-2}$ for PDMS-CNT implants. The estimated peak-
413 to-peak acoustic pressures at the surface of the implants were 0.05 MPa and 0.15 MPa for
414 PDMS/CS/PDMS and PDMS-CNT implants, respectively. We observed activation in a large cSC area
415 following each photoacoustic stimulation (Fig. 7d-e) using both types of implants (Fig. 7c, iii).
416 Photoacoustic stimulation with the PDMS/CS/PDMS and PDMS-CNT implants activated cSC areas
417 measuring 25 ± 4 % (n = 4) and 38 ± 10 % (n = 5) of the full-field-white-light-activated area, respectively
418 (Fig. 7f). Furthermore, in the 29-by-29-pixel ROI, the averaged rCBV amplitudes for the

419 PDMS/CS/PDMS (Fig. 7g, blue) and PDMS-CNT (Fig. 7g, black) implant stimulations reached similar
420 amplitudes to that generated with the 400-µm-diameter spot of the 565-nm laser light on the healthy
421 retina (Fig. 7g, orange). The size of the activated areas generated by stimulation with the
422 PDMS/CS/PDMS and PDMS-CNT implants, and with the 595-nm-laser spot, were not significantly
423 different (Fig. 7f). By contrast, a direct 1030-nm-light stimulation of the healthy retina (Fig. 7c, iv; P =
424 0.56 ± 0.21 $W.mm^{-2}$, 400-µm-diameter spot) did not generate a significant cSC activation (Fig. 7f). The
425 averaged rCBV was negligible in the ROI, and statistically different from all of the other measurements
426 (Fig. 7g, dark red). Taken together, these results show that the photoacoustic stimulation of the
427 degenerated retina elicits a robust and local activation of the visual pathway downstream of the
428 retina, with an amplitude and size comparable to a visible light stimulation of the retina.

429

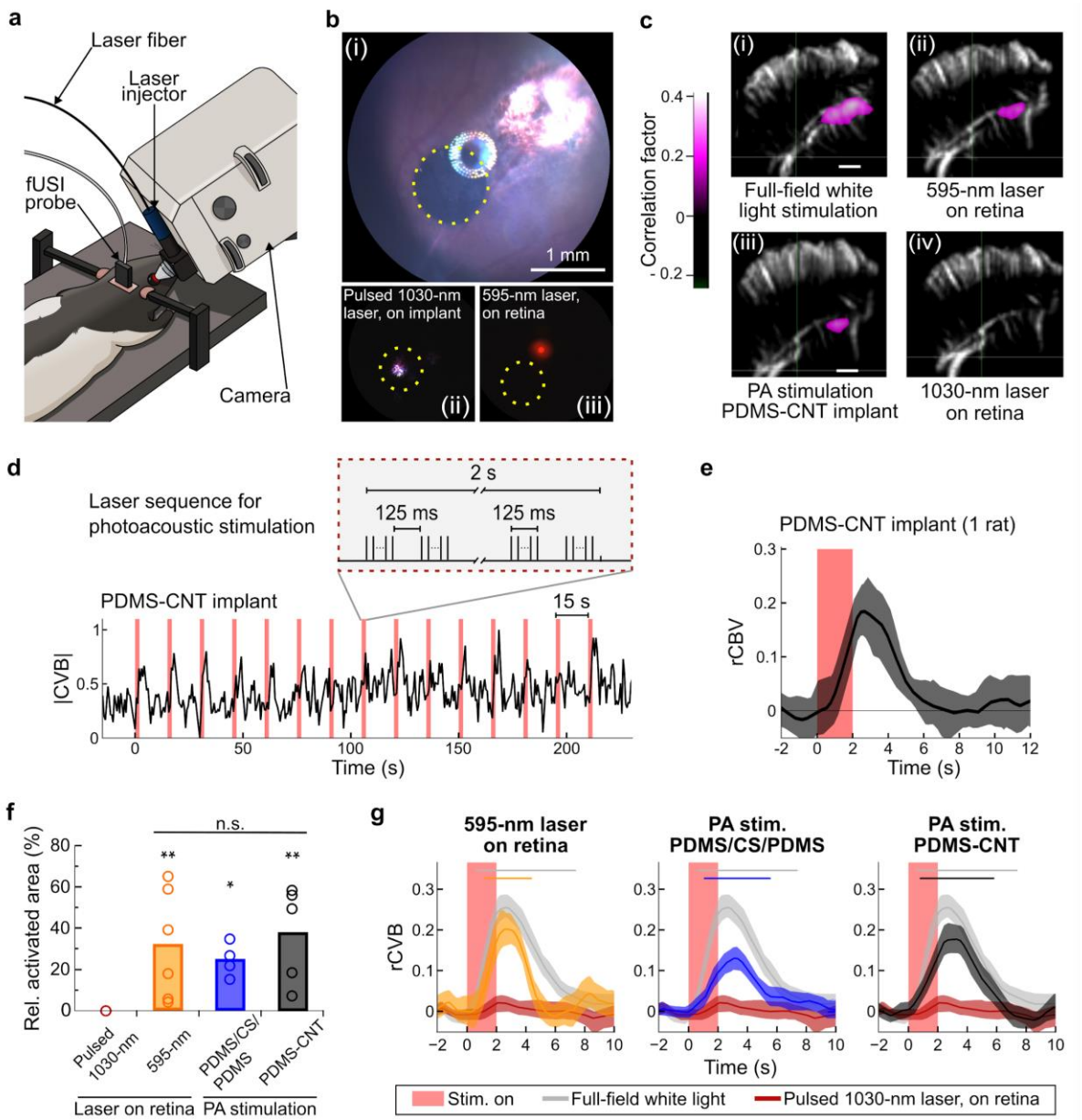

Figure 7. Superior colliculus activation following photoacoustic stimulation of *in vivo* LE retinae. (a) Setup for *in vivo* eye stimulation and fUSI recordings. **(b)** Eye fundus images of a 1-mm PA implant (*i,* yellow dotted circle) and 400-µm-diameter laser spots (*ii*: pulsed 1030-nm laser on the implant, *iii*: continuous 595-nm laser on the retina) used for laser and photoacoustic stimulation. **(c)** Functional ultrasound imaging in the coronal plane (left hemisphere, AP, -6.5 mm from the bregma). The correlation map displays the relationship between relative cerebral blood volume (rCBV) and the stimuli. Active pixels reflect regions of activated neurons in the contralateral superior colliculus (cSC) for a single recording (15 stimulations). **(d)** Top: Laser sequence for photoacoustic stimulation (repetition rate f_{rep} = 6.1 kHz). Bottom: example normalized CBV trace for pulsed 1030-nm

441 photoacoustic stimulation on a PDMS-CNT implant (measured in 29-by-29-pixel region of interest of
442 the cSC, chosen as the area with peak correlation to full-field-white-light stimulation). Baseline activity
443 was recorded for 40 s before and after the stimulation session, and was used to normalize the CBV
444 signal. **(e)** Average rCBV for a single session with 15 stimulations (same data as for (d)). Mean rCBV ±
445 99% CI. The laser sequence starts at 0 s. Red shaded area: PA stimulation. **(f)** Activated area following
446 stimulation, relative to the area activated by full-field white light stimulation (rel. activated area), for
447 different stimuli: full-field white light stimulation (light gray, 6 rats, n = 6 recordings), 1030-nm laser
448 stimulation on the retina (dark red, 3 rats, n = 4 recordings), 595-nm laser stimulation on the retina
449 (orange, 3 rats, n = 6 recordings), photoacoustic stimulation with PDMS/CS/PDMS implant (blue, 3
450 rats, n = 4 recordings), and photoacoustic stimulation with PDMS-CNT implant (black, 2 rats, n = 5
451 recordings). The activated area is measured by counting the number of pixels on correlation maps
452 such as (c). Circles on the graph mark the ratio for individual recordings. Statistics: p-values vs white
453 light stimulation: * $p < 0.05$, ** $p < 0.01$, Wilcoxon Signed-Rank test. PDMS/CS/PDMS vs 595 nm: $p =$
454 0.91, PDMS-CNT vs 595 nm: $p = 0.792$, PDMS/CS/PDMS vs PDMS-CNT: $p = 0.56$, Mann-Whitney U test.
455 **(g)** Mean rCBV responses of individual rats following stimulation with a laser (595-nm and 1030-nm
456 on retina) and photoacoustic stimulation, for all rats. Same data as (f). Horizontal bars denote
457 significant elevation with respect to the baseline (e.g., no overlap of CI with basal CI). No significant
458 difference in rCVB following photoacoustic stimulation between both implant types was found (e.g.,
459 overlapping confidence intervals). Peak rCBV values: white light, 0.26 (at 2.65 s); 595 nm, 0.20 (at 2.69
460 s); PDMS-CNT, 0.18 (at 3.24 s); PDMS/CS/PDMS, 0.13 (at 3.18 s); 1030-nm laser on retina, 0.02 (at 2.19
461 s). Shaded areas: 95% bootstrapped CI. Red shaded area: PA stimulation.

462

463 ## Discussion

464 In this study, we developed flexible photoacoustic films that efficiently generated acoustic waves.
465 Although CS-PDMS films have been developed as laser ultrasound transducers[23–25] and for
466 superhydrophobic coating[26,27], our study represents the first instance of engineering them into a
467 sandwich-structured PDMS-CS-PDMS film as a biomedical implant, specifically designed to minimize
468 heat deposition in the surrounding tissue and to minimize the diffusion of carbon particles into the
469 biological tissue. The generated photoacoustic waves successfully stimulated the activity of retinal
470 cells *ex vivo* and *in vivo*, thereby activating downstream visual pathways *in vivo*. This RGC stimulation
471 was demonstrated both *ex vivo* and *in vivo* on degenerated retinae. These results therefore provide
472 evidence that the degenerated retina maintains some ultrasound sensitivity, enabling RGC activity
473 modulation and the consecutive stimulation of higher visual areas for visual restoration.

474 We showed that an acoustic pressure of 0.05 MPa was sufficient to elicit responses in the superior
475 colliculus, which is two orders of magnitude lower than the pressure thresholds previously reported
476 for *in vivo* transducer-based ultrasound retinal stimulation[9]. Pressure thresholds of photoacoustic
477 stimulation correspond to mechanical indexes (MI) below 0.03 (PDMS/CS/PDMS film) and 0.1 (PDMS-
478 CNT film) and spatial peak temporal average intensities (I_{SPTA}) below 0.06 and 0.9 $mW.cm^{-2}$,
479 respectively (Supplementary Table T1). Temperature increases were measured to be below 1 °C at the
480 film surface (Fig. 1g, Supplementary Fig. S6). These metrics align with FDA safety guidelines for
481 ultrasonic ophthalmic devices[28], making our PA implants a promising option for safe ultrasound
482 stimulation of the retina. Due to the bidirectional nature of our implant, acoustic waves are
483 transmitted not only to the retinal side, but also to the opposite side toward the RPE and choroid,
484 potentially impacting mechanosensitive elements therein. While the implications of ultrasound waves
485 to the RPE and choroid require further investigation, the applied acoustic pressures are below safety
486 thresholds and the acoustic waves are applied at 0.025% duty cycle. Thus limited or no aversive effects
487 are to be expected on the RPE and choroid.

488 Restoring meaningful vision requires high spatial resolution over a large area of the retina. To achieve
489 this, each individual stimulation source (pixel) must produce tightly confined fields with sub-20-µm[29]
490 lateral resolution, and maximize pixel density to 2500 $px.mm^{-2}$ in the macula, which covers a 25 mm^2
491 area in humans. Among current electrical retinal prostheses, complex 3D honeycomb photovoltaic
492 devices[32] and optimized laser stimulation sequences[33] show potential to generate 20-µm-wide electric
493 fields with dense arrays of thousands of electrodes, but each rigid implant can only cover at best 9
494 mm^2 of the retina. Ultrasound retinal stimulation offers the advantage of non-invasive stimulation
495 over an area greater than the macula, but the pixel density of transducer 2D-arrays is very limited

496 (currently 16 x 16[9]) regardless of the lateral resolution of the stimulation field, which remains above
497 80 µm (*in silico* data, at 20 MHz[9]). The photoacoustic film demonstrated in this study offers the
498 potential to meet both of these needs due to its spatially continuous nature and the multiplexing
499 capability of photons. We demonstrated through PA-field mapping that a 50-µm-diameter laser spot
500 generates a 56-µm lateral ultrasound field, and that the RGC activity was locally modulated around
501 the laser spot in both healthy and degenerated retinae. Neuronal spatial resolution based on MEA
502 recordings still remains to be determined. Additionally, the potential of the photoacoustic film to
503 enable high visual acuity using smaller laser spot sizes is currently under investigation. Moreover, the
504 pixel number could exceed a million by using digital micromirror devices to project a laser pattern
505 onto the continuous film. Whole-eye models will be necessary to predict the actual resolution that
506 could be achieved for *in-human* applications. A comparison between our approach and other vision
507 restoration technologies across multiple parameters is summarized in Supplementary Table T2.

508 Since the structures involved in retinal mechanosensitivity are not yet known, it is difficult to evaluate
509 the potential adaptation or depression of mechanosensitivity to long-term ultrasonic retinal
510 stimulation for vision restoration. It has been shown that retinal stretch with increased intraocular
511 pressure (IOP) resulted in an increased expression of Piezo1 and 2 in RGCs[25]. While the similarities
512 between the mechanisms underlying elevated IOP and ultrasonic mechanostimulation are not yet
513 understood, it is conceivable that ultrasonic mechanostimulation may also lead to an increase in the
514 expression of mechanosensitive proteins. In the course of our studies, no such depression was
515 observed, but the stimulations were limited in time. Future studies need to be conducted to better
516 evaluate the effect of long-term mechanical stimulation of the retina.

517 While further studies are required to investigate the mechanisms of photoacoustic retinal stimulation
518 and whether the implant can restore meaningful vision to patients afflicted by retinal degenerative
519 diseases, our results collectively demonstrate that photoacoustic retinal stimulation through flexible
520 implants opens up potential for an innovative strategy for restoring vision, with high precision and a
521 large field of view.

522 ## Material and methods

523 **Design of the photoacoustic film**

524 Both the laser wavelength and the PA materials were optimized for safety and performance. Light
525 wavelengths ranging from 500 nm to 1150 nm have maximum transmission in the human eye media[34].
526 A nanosecond laser with a 1030-nm wavelength was chosen to maximize transmission to the retina[34],
527 while avoiding triggering responses in photoreceptors, as AMD patients may retain peripheral vision.
528 CS and CNT were selected as the absorber material due their high photoacoustic conversion efficiency,
529 accessibility, and lower safety concerns compared to lead-containing materials[35,36]. For the thermal
530 expansion material, PDMS was identified as the best option due to its transparency, high Grüneisen
531 parameter, excellent biocompatibility, and stability[37]. Although CS-PDMS films have been developed
532 as laser ultrasound transducers[23–25], our study represents the first instance of engineering them into
533 a sandwich-structure. The PDMS mixing ratio was adjusted to 5:1 to increase the Young's modulus,
534 thereby enhancing photoacoustic conversion efficiency[38]. The central frequency of our film is an
535 intrinsic property of our film under our given experimental conditions. Several factors influence the
536 ultrasound frequency generated by a photoacoustic device, including the laser pulse duration, the
537 Grüneisen parameter of the elastomer material, and the effective optical absorption depth. In our
538 setup, the laser pulse duration is fixed, PDMS is the only choice of absorber because it is both
539 transparent and exhibits a high Grüneisen parameter, and the concentration of the CS layer remains
540 constant due to the constraints of the flame synthesis process.

541 **Fabrication of the photoacoustic films**

542 To fabricate the 115-µm-thick PDMS/CS/PDMS film, a uniform layer of candle soot was flame-
543 synthesized and deposited onto a glass slide for 20 s, achieving a thickness of approximately 4 µm.
544 Subsequently, a degassed PDMS mixture of silicone elastomer base and curing agent (Sylgard 184,
545 Dow Corning Corporation, USA) with mix ratios of 5:1 was spin-coated at 500 rpm onto the candle
546 soot layer, and cured at 110 °C for 15 minutes. The resulting cured film was then detached from the
547 glass slide, inverted, and reattached. Another layer of PDMS mixture was spin-coated at 500 rpm and
548 cured at 110 °C for 15 minutes.

549 To fabricate the 40-µm-thick PDMS-CNT film, we employed a recipe derived from previous work[10]. We
550 initially prepared PDMS at mix ratios of 10:1. Subsequently, a 15%wt of CNT (<8 nm OD, 2–5 nm ID,
551 length 0.5–2 µm, VWR, Inc., USA) was mixed with the PDMS, with the addition of IPA to facilitate CNT
552 dissolution. The resulting mixture underwent a 5-minute sonication process, followed by a 30-minute

553 degassing step to eliminate bubbles and IPA. The prepared mixture was then spin-coated onto a glass
554 substrate at 500 rpm for 5 minutes. The coated substrate was cured at 110 °C for 15 minutes.

555 Both PDMS/CS/PDMS and PDMS-CNT films were treated with oxygen plasma for 1 min on both sides,
556 to make the implant surface hydrophilic[39]. This allows for better cell adhesion, which reduces the risks
557 of film displacement after the implantation surgery. The film was cut into smaller areas (5 x 5 cm^2) and
558 stored in distilled water before use to avoid reversion to their hydrophobic state. Biopsy punches
559 (Kaimedical) of 1 mm and 1.5 mm were used to cut individual photoacoustic films for *ex vivo* and *in*
560 *vivo* experiments.

561 **Characterization of the photoacoustic properties of the films**

562 The photoacoustic properties of the films were characterized with a 40-µm needle hydrophone system
563 (NH0040, Precision Acoustics Inc., UK) or an 85-µm needle hydrophone system (HGL-0085, Onda
564 Corporation, USA). Illumination was provided by a Q-switched diode-pumped laser with a pulse width
565 of 8 ns (RPMC, wavelength 1030 nm, repetition frequency 2.9 kHz, USA), delivered to one side of the
566 film via a multimode fiber with a 200-µm core (FT200UMT, Thorlabs, USA). On the other side of the
567 film, the hydrophone was mounted on a 3D stage and aligned with the area illuminated by the optical
568 fiber. The signals were amplified with a pulser-receiver (Olympus, Model 5073PR, USA) and then
569 recorded via a digital oscilloscope (Rigol, DS4024, USA).

570 **Mapping the photoacoustic pressure field**

571 Photoacoustic field microscopy was used to map the generated ultrasound field (Supplementary Fig.
572 S7), as previously reported[40]. Here a 1064-nm pulsed laser (OPOLETTE 355 LD, OPOTEK, pulse duration
573 5 ns) was used as the pump beam. A continuous wave 1310-nm laser (1310LD-4-0-0, AeroDIODE
574 Corporation) served as the probe. A piece of PDMS/CS/PDMS film was mounted on a 50-µm optical
575 fiber (FG050UGA, Thorlabs), and the 1064-nm laser was delivered to the film sample to generate the
576 photoacoustic signals. A translation stage (ProScan III, Prior) was used to scan the generated
577 ultrasound field. Under a single ns pulse, the PA-induced refractive index change was detected as the
578 imaging contrast.

579 **Temperature measurements**

580 A J-type thermocouple with a 200-µm tip was set against the PDMS/CS/PDMS film inside 3% agarose
581 gel, typically used for mimicking tissue[41]. The PDMS/CS/PDMS film was attached to a 200-µm optical
582 fiber to assure the alignment between the illuminated area on the film and the thermocouple tip. A
583 Q-switched diode-pumped laser with a pulse width of 4.5 ns (RPMC, wavelength 1030 nm, USA) was

584 used to illuminate the film. The temperature on the film was recorded with a 2 kHz sampling rate from
585 10 recordings. Average data was computed from the 3 recordings that showed the highest
586 temperature rise. Photos of the setup are shown in Supplementary Fig. S5. No transient temperature
587 events faster than the 2 kHz acquisition frequency are expected to occur (Supplementary Fig. S6).

588 **Animals**

589 All animal experiments were conducted at the Paris Vision Institute, in accordance with the National
590 Institutes of Health Guide for the Care and Use of Laboratory animals. Protocols were approved by the
591 Local Animal Ethics Committee (Committee Charles Darwin CEEACD/N°5, project reference
592 Apafis#40263-2023010909277429 v5) and conducted in agreement with Directive 2010/63/EU of the
593 European Parliament. Wild-type Long-Evans male rats aged between 2 and 8 months were obtained
594 from Janvier Laboratories. P23H male and female transgenic rats (9-14 months old) were raised locally.
595 P23H rats serve as a model for autosomal dominant retinitis pigmentosa[42].

596 ***Ex vivo* experiments**

597 ***Ex vivo* retina preparation and blockers**

598 The following procedures were carried out under dim red light. Animals were dark adapted for 30
599 minutes, then anesthetized with CO_2 and euthanized by cervical dislocation. The eyes were enucleated
600 and hemisected in carboxygenated (95% O_2, 5% CO_2) Ringer medium containing (in mM): 125 NaCl,
601 2.5 KCl, 1 $MgCl_2$, 1.25 NaH_2PO_4, 20 glucose, 26 $NaHCO_3$, 1 $CaCl_2$ and 0.5 L-Glutamine at pH 7.4. The
602 medium was continuously perfused in the recording chamber at a speed of 1.5 $mL.min^{-1}$ and was kept
603 around 37 °C.

604 Isolated retinae were placed on a dialysis membrane (Spectra/Por® 6 50 kD dialysis membrane,
605 Spectrum) coated with poly-L-lysine (0.1%, Sigma), with the photoacoustic film between the dialysis
606 membrane and the retina, and with photoreceptors against the film. The retinae were pressed against
607 a multi-electrode array (MEA) (MEA256 iR-ITO; Multi-Channel Systems, Reutlingen, Germany) with a
608 custom 3D-printed piece.

609 Pharmacological blockers were bath-applied through the perfusion line. AMPA/kainate glutamate
610 receptor antagonist 6-cyano-7-nitroquinoxaline-2,3-dione (CNQX, 20 µM, Tocris Bioscience) and
611 NMDA glutamate receptor antagonist (RS)-3-(2-carboxypiperazin-4-yl)-propyl-1-phosphonic acid
612 ((RS)-CPP, 10 µM, Tocris Bioscience) were used to block signaling upstream of RGCs and therefore
613 isolate the contribution of RGCs in PA-induced responses. Group III metabotropic glutamate receptor
614 agonist L-(+)-2-Amino-4-phosphonobutyric acid (L-AP4, 20 µM, Tocris Bioscience) was used to block

615 the signaling between photoreceptors and ON bipolar cells[43] to better understand the contribution of
616 photoreceptors in retinal mechanosensitivity. Kainate antagonist (*S*)-1-(2-Amino-2-carboxyethyl)-3-
617 (2-carboxy-5-phenylthiophene-3-yl-methyl)-5-methylpyrimidine-2,4-dione was used to block
618 remaining PA responses after L-AP4 application.

619

620 ***Ex vivo* photoacoustic retinal stimulation**

621 Photoacoustic stimulations were done with a 1030-nm, 4.2-ns-pulsed laser (One DPSS, Bright
622 Solutions) delivered through a 200-µm-core 0.22 NA multimode SMA/SMA optic fiber (Thorlabs Inc,
623 USA., ref M25L01). A second 200-µm-core was connected to the first fiber using a fixed attenuator
624 (Thorlabs Inc., USA, ref FA26M) to control the power density. The optical fiber was inserted into a
625 custom 3D-printed holder incorporated in a motorized XYZ stage with 5-nm precision (Sensapex, uMp-
626 3 micromanipulator). It was lowered above the PA film at a ~90° angle and placed at a fixed (~ 1 mm)
627 distance above the PA film. The illumination spot was measured ~300 µm in diameter on the film using
628 ImageJ and the MEA electrode pitch as reference. A low power 650-nm guiding beam (FIBERCHECK,
629 Laser Components) was used to calibrate the beam position relative to the MEA.

630 Laser pulse repetition rate and the laser burst trains were controlled using a Teensy microcontroller
631 custom written software (C++, Java, Python). In a typical stimulation, the laser delivered 10 µJ pulses
632 with a repetition frequency f_{rep} of 1.9 kHz or 3.5 kHz during a single 5-ms to 30-ms burst, repeated at
633 1 Hz for 40 bursts. PA film integrity was confirmed by the lack of photoelectric effect in the MEA
634 recordings (Supplementary Fig. S8).

635 **Analysis of MEA recordings**

636 MEA raw traces were recorded through the MEA software (MC Rack, Multichannel Systems). Spikes
637 were sorted using SpyKING CIRCUS[44], manually curated using phy[45], and attributed to individual cells.
638 Spikes were referenced relative to stimulus onset and grouped across trials in bins using a sliding
639 window (bin width = 20 ms, increments = 5 ms). Cell activity in each bin was estimated using bootstrap
640 resampling (n = 1000 resamples, 99% confidence intervals), and considered significantly increased or
641 decreased if there were no overlapping confidence intervals compared to baseline (200 - 100 ms
642 before stimulus onset).

643 RGCs were considered responsive or modulated if their firing rate was significantly increased or
644 decreased compared to baseline for at least 15 ms consecutively, and response latency was defined
645 as the first bin of this series. Noise clusters were filtered from the cell clusters by excluding cells with

646 response latencies below 5 ms. A 300-µm-diameter area was illuminated by the 1030-nm laser (200-
647 µm fiber) during photoacoustic stimulation. For quantifying responsive cells and dose responses (Fig.
648 2 and 3), we included only cells within 300-µm of the center of the illuminated area ("stimulation
649 site"). The number of recorded cells per stimulation site is shown in Supplementary Fig. S9. Cells with
650 a response latency above 250 ms were excluded, as they were likely not a result from direct
651 stimulation.

652 To analyze the relation between cell modulation and distance from the stimulation area (Fig. 5a), we
653 calculated local averages in firing rate by assigning the firing rate of each cluster to a bin in a grid with
654 a spacing of 25 µm, and smoothing the resulting averages using a convolution with a gaussian kernel
655 (sigma = 100 µm).

656 ***In vivo* experiments**

657 Successful implantation was defined as good positioning of the 1-mm-diameter film in the subretinal
658 space, with no complications due to surgery. N = 8 adult (9-10 mo) P23H rats were successfully
659 implanted and used for biocompatibility studies. N = 7 adult Long-Evans rats were successfully
660 implanted at 8 weeks of age and used for photoacoustic stimulation.

661 **Surgery procedures for chronic subretinal implantation**

662 A 1-mm-diameter PA film was surgically placed in the subretinal space in the central region next to
663 the optic nerve, as previously described[31]. Briefly, a small sclerotomy was performed on the dorsal
664 sclera tangential to the cornea. A gel of sodium chondroitin sulfate-sodium hyaluronate (Viscoat
665 Alcon) was injected in the sclerotomy to generate a retinal detachment. The implant was then inserted
666 below the detached retina in the subretinal space, targeting a location adjacent to the optic disk.

667 **Ocular imaging**

668 Eye fundus imaging (MICRON® IV, Phoenix, USA) and optical coherence tomography (Bioptigen® OCT
669 system, Leica microsystems, Germany) were performed at 7 and 15 days post-implantation (dpi) for
670 all rats to monitor inflammation and confirm correct implantation. Additional imaging was conducted
671 at 30, 60, 90 and 120 dpi for rats that did not undergo prior retinal stimulation.

672 **Cranial window acute surgery**

673 Anesthesia was provided with an intraperitoneal injection of 40 $mg.kg^{-1}$ ketamine (Axience, France)
674 and 0.14 $mg.kg^{-1}$ medetomidine (Domitor®, Vétoquinol, France) diluted in sodium chloride. The animal
675 was placed on a stereotaxic frame to perform a left craniotomy. Drops of ocular gel (Lubrithal®,

676 Dechra, France) were applied and the eyes were then covered with a black cloth for dark adaptation.
677 A rectangular piece of bone was removed from Bregma -3 mm to -8 mm.

678 **Retinal stimulation and brain imaging**

679 Retinal stimulation was performed 26 - 40 days after implantation surgery for rats with
680 PDMS/CS/PDMS implants and 23 - 29 days after implantation surgery for PDMS-CNT implants, and
681 immediately after the cranial window surgery. Anesthesia was re-administered every 45 min with one-
682 third of the initial dose, up to a maximum of 5 injections. At the end of the experiment, the animals
683 were euthanized using an intracardiac injection (Exagon®, Axience, France).

684 For full field light stimulations with a white LED source, the light power on the retina was estimated
685 to be ~0.02 $mW.mm^{-2}$, based on the power entering the pupil of 1.2 mW. The choice of the stimulation
686 protocol was informed by prior retina studies using functional ultrasound imaging[31,46]. Each 1.8-s
687 stimulation sequence consisted of 6 evenly spaced 300-ms illuminations (LED on), repeated 15 times.

688 For 595-nm, 1030-nm light stimulation and photoacoustic stimulation, focused laser spots were aimed
689 using a laser injector from the MICRON® 810-nm Image-Guided Laser modality combined with a
690 MICRON® III camera (Phoenix, USA). A low power 650-nm guiding beam (FIBERCHECK, Laser
691 Components) was coupled to the injector to safely choose the area to stimulate. The rat's implanted
692 eye was covered in ocular gel (Lubrithal®, Dechra, France) and in contact with the camera lens.
693 Stimulation sequences for all 3 modalities were identical.

694 For 595-nm (continuous) laser stimulation, power density on retina was 26 µW in a 400 ± 26 -µm-
695 diameter laser spot. For photoacoustic stimulation, the same 1030-nm pulsed laser used in the *ex vivo*
696 experiments was employed. The laser energy exiting the laser injector was E_p = 15 µJ per pulse. To aim
697 at the implant for photoacoustic stimulation, the laser focal spot was not placed on the optical axis of
698 the injector lens, which resulted in a loss of power. All the laser diameter at $1/e^2$ (D_L) and laser power
699 density P were estimated from average intensity profiles extracted with Fiji/ImageJ (Supplementary
700 Fig. S10 and S11) and are expressed as the mean ± standard deviation.

701 For 1030-nm laser stimulation on the retina: D_L = 470 ± 70 µm. P = 0.56 ± 0.21 $W.mm^{-2}$,
702 for 1030-nm photoacoustic stimulation with PDMS-CNT implants: D_L = 360 ± 60 µm. P = 0.39 ± 0.12
703 $W.mm^{-2}$,
704 for 1030-nm photoacoustic stimulation with PDMS/CS/PDMS implants: D_L = 410 ± 45 µm. P = 0.29 ±
705 0.06 $W.mm^{-2}$.

706 The pupil of the eye of interest was dilated with a tropicamide-based eye drop solution (Mydriaticum®,
707 Théa, France) before the first recording. Body temperature was monitored with a rectal probe and
708 maintained using a heating blanket. Respiratory and heart rates were continuously monitored (TCMT,
709 Minerve, France). After local application of lidocaine (4 $mg.kg^{-1}$, Laocaïne®, MSD, France), the thinned
710 skull was exposed and covered with ultrasound gel. The rats were scanned with a system dedicated
711 to small animal ultrasound neuroimaging (Iconeus, Paris, France). Doppler vascular images were
712 obtained using the Ultrafast Compound Doppler Imaging technique[47]. The probe was positioned
713 coronally at Bregma - 6.5 mm in order to measure the cerebral blood volume (CBV) in the contralateral
714 superior colliculus. Each frame was a compound plane wave frame[48] resulting from the coherent
715 summation of backscattered echoes obtained after successive tilted plane waves emissions. Then, the
716 CBV signal was extracted from the tissue signal by filtering the image stacks with a dedicated
717 spatiotemporal filter using Singular Value Decomposition[49]. Each transcranial Power Doppler image
718 was obtained from 200 compounded frames acquired at 500 Hz frame rate.

719 **Immunohistochemistry and image acquisition**

720 After euthanasia, the eyes (n = 3 LE rats, n = 4 P23H rats) were enucleated and fixed with 4%
721 paraformaldehyde (Cat no. 100496, Sigma-Aldrich) in 0.1 M phosphate buffer for 1 hour. The retinae
722 were dissected and incubated in blocking solution (0.3% Triton X100 (Cat no. X100-500ML, Sigma-
723 Aldrich), 10% Horse Serum (26050-070, Gibco) in phosphate buffer) with the primary antibodies (Iba1
724 (AB48004, Abcam), GFAP (Z0334, Dako), rhodopsin (MAB5316, Merck Millipore), cone arrestin
725 (AB15282, Merck Millipore) for three days at room temperature. The secondary antibodies used to
726 detect immunolabeling were goat anti-IgG conjugated to Alexa-Fluor 488, 594 or 647 (A212026,
727 A21203, and A21447, Invitrogen).

728 The retinae were flat-mounted, and imaged using an Olympus FV3000 confocal microscope with a 20X
729 objective (UPLXAPO20X NA 0.8 WD 0.6, Evident).

730

731 **Analysis of *in vivo* experiments**

732 **Analysis of OCT images**

733 Mean retinal thickness next to and above the implant were measured with ImageJ on OCT images
734 (diametral slices). The number of rats imaged at 30 dpi and later was lower than the number imaged
735 at 7 dpi and 15 dpi because rats were used for terminal retinal stimulation recordings starting at 23
736 dpi.

Analysis of functional ultrasound imaging recordings

The correlation map of the CBV variations and the laser sequence for stimulation was computed by the manufacturer's proprietary IcoStudio software (v1.5.2). A delay of either 2 or 3 s was computed in the calculation of the correlation to account for vascular delay (the chosen value maximizes the correlation). In correlation map displays (Fig. 7c), only significant pixels with a correlation threshold greater than 0.2 are shown. Maps with a correlation threshold of 0.1 are shown in Supplementary Fig. S12. A 29-by-29-pixel (29 pixels = 302 ± 10 µm) region of interest (ROI) was defined for each animal, centered on the peak intensity of the correlation map for full-field-white-light stimulation. Relative CBV variations (rCBV) were extracted in this ROI for all stimulation types. For each recording (15 laser stimulations), the cerebral blood flow (CBV) was normalized into a relative steady-state value (rCBV) and calculated as the following: $rCBV = (CBV(t) - CBV_0)/CBV_0$, where CBV(t) is the power doppler value t seconds after the start of laser sequence, and CBV_0 is the baseline in the ROI. The baseline was defined as the mean power doppler value 5 seconds before the start of the laser sequence. The data was bootstrapped to calculate confidence intervals.

Statistical analysis

Values are expressed as mean values ± standard error of the mean (SE) in figures and in the text, unless specified otherwise. Similarly, in scatter plots with error bars (Fig. 1, Fig. 4), data points and error bars represent the mean and the standard error of the mean, respectively.

Data normality was checked with SciPy normaltest. Data did not follow a normal distribution. Statistical significance was analyzed with Wilcoxon signed-rank tests and Mann-Whitney U tests (Fig. 2 to 6). Pearson correlation (Fig. 2 to 4) was computed to quantify the strength and direction of the linear relationship between two continuous variables. One-way ANOVA was used to test the effect of a single factor on the mean of a dependent variable (Fig. ~~5~~ 6). Finally, to estimate confidence intervals for a statistic of unknown distribution (average rCBV variations in Fig. 7) we used bootstrapped estimation (1000 samples, 95% confidence intervals). Statistical tests are provided in the figure legends.

Acknowledgements

This work was supported by the National Institute of Health, United States, through the BRAIN Initiative (BRAIN/NEI R21 EY035437 and NEI 1R21EY036579) to CY, by the Foundation Fighting Blindness (PPA-0922-0840-INSERM) to SP, by IHU FOReSIGHT, France, (ANR-18-IAHU-01) to SP, by the

European Research Council (Grant Agreement 101045289) to SP, and by Axorus SAS, France, to SP and CY.

Competing interests

This study was funded in part by the company Axorus SAS. J-DL and HM are major stakeholders in Axorus. CY and J-XC are minor stakeholders in Axorus.

Author Contributions

Equal contributions: A.L., Y.L. and TR.R, and S.P. and H.M.

A.L., Y.L., TR.R. and H.M. designed the experiments.

A.L., Y.L., TR.R., H.M., C.B., J.V., A.F., C-A.C., G.C., Y.Y., C.J., M.C. and J.D. carried out the experiments and analyzed the data.

J-D.L. and G.T. provided support for the experiments, study design and data analysis.

H.M., J-D.L., J-X.C., C.Y. and S.P. conceived the project, and contributed to study design and data interpretation.

A.L., Y.L., TR.R., C.Y.,H.M., and S.P. wrote the manuscript with input from all others.

Data availability

Data are available from the corresponding author upon reasonable request.

Code availability

The custom Python codes are available from the corresponding author upon request.

791 ## References

792 1. Jeany Q Li *et al.* Prevalence and incidence of age-related macular degeneration in Europe: a
793 systematic review and meta-analysis. *Br. J. Ophthalmol.* **104**, 1077 (2020).
794 2. Da Cruz, L. *et al.* Five-Year Safety and Performance Results from the Argus II Retinal Prosthesis
795 System Clinical Trial. *Ophthalmology* **123**, 2248–2254 (2016).
796 3. Wu, K. Y., Mina, M., Sahyoun, J.-Y., Kalevar, A. & Tran, S. D. Retinal Prostheses: Engineering and
797 Clinical Perspectives for Vision Restoration. *Sensors* **23**, 5782 (2023).
798 4. Muqit, M. M. K. *et al.* Prosthetic Visual Acuity with the PRIMA Subretinal Microchip in Patients
799 with Atrophic Age-Related Macular Degeneration at 4 Years Follow-up. *Ophthalmol. Sci.* **4**,
800 (2024).
801 5. Lu, G. *et al.* Ultrasound Retinal Stimulation: A Mini-Review of Recent Developments. *IEEE Trans.*
802 *Ultrason. Ferroelectr. Freq. Control* **69**, 3224–3231 (2022).
803 6. Menz, M. D., Oralkan, Ö., Khuri-Yakub, P. T. & Baccus, S. A. Precise Neural Stimulation in the
804 Retina Using Focused Ultrasound. *J. Neurosci.* **33**, 4550–4560 (2013).
805 7. Gong, C. *et al.* Non-Invasive Hybrid Ultrasound Stimulation of Visual Cortex In Vivo.
806 *Bioengineering* **10**, 577 (2023).
807 8. Qian, X. *et al.* Noninvasive Ultrasound Retinal Stimulation for Vision Restoration at High
808 Spatiotemporal Resolution. *BME Front.* **2022**, 9829316 (2022).
809 9. Lu, G. *et al.* Noninvasive imaging-guided ultrasonic neurostimulation with arbitrary 2D patterns
810 and its application for high-quality vision restoration. *Nat. Commun.* **15**, 4481 (2024).
811 10. Shi, L. *et al.* Non-genetic photoacoustic stimulation of single neurons by a tapered fiber
812 optoacoustic emitter. *Light Sci. Appl.* **10**, 143 (2021).
813 11. Du, Z. *et al.* Photoacoustic: A Versatile Nongenetic Method for High-Precision Neuromodulation.
814 *Acc. Chem. Res.* **57**, 1595–1607 (2024).
815 12. Jiang, Q. *et al.* Temporal Neuromodulation of Retinal Ganglion Cells by Low-Frequency Focused

816 Ultrasound Stimulation. *IEEE Trans. Neural Syst. Rehabil. Eng.* **26**, 969–976 (2018).

817 13. Lee, H. C. *et al.* Histological evaluation of flexible neural implants; flexibility limit for reducing the
818 tissue response? *J. Neural Eng.* **14**, 036026 (2017).

819 14. Andersen, M. A. & Schouenborg, J. Polydimethylsiloxane as a more biocompatible alternative to
820 glass in optogenetics. *Sci. Rep.* **13**, 16090 (2023).

821 15. Menz, M. D. *et al.* Radiation Force as a Physical Mechanism for Ultrasonic Neurostimulation of
822 the *Ex Vivo* Retina. *J. Neurosci.* **39**, 6251–6264 (2019).

823 16. Zhuo, S.-Y. *et al.* Mechanism of low-frequency, low-intensity ultrasound modulation of the
824 mouse retina. *J. Neural Eng.* **20**, 036025 (2023).

825 17. Chen, G. *et al.* High-Precision Photoacoustic Neural Modulation Uses a Non-Thermal
826 Mechanism. *Adv. Sci.* **11**, 2403205 (2024).

827 18. Palczewska, G. *et al.* Human infrared vision is triggered by two-photon chromophore
828 isomerization. *Proc. Natl. Acad. Sci.* **111**, (2014).

829 19. Vinberg, F. *et al.* Sensitivity of Mammalian Cone Photoreceptors to Infrared Light. *Neuroscience*
830 **416**, 100–108 (2019).

831 20. Rabell-Montiel, A., Anderson, T., Pye, S. D. & Moran, C. M. Attenuation Coefficients of the
832 Individual Components of the International Electrotechnical Commission Agar Tissue-Mimicking
833 Material. *Ultrasound Med. Biol.* **44**, 2371–2378 (2018).

834 21. Lorach, H. *et al.* Development of Animal Models of Local Retinal Degeneration. *Investig.*
835 *Opthalmology Vis. Sci.* **56**, 4644 (2015).

836 22. Prévot, P.-H. *et al.* Behavioural responses to a photovoltaic subretinal prosthesis implanted in
837 non-human primates. *Nat. Biomed. Eng.* **4**, 172–180 (2019).

838 23. Chang, W.-Y. *et al.* Photoacoustic transduction efficiency evaluation of candle soot
839 nanoparticles/PDMS composites. in *2017 IEEE 17th International Conference on Nanotechnology*
840 *(IEEE-NANO)* 439–442 (2017). doi:10.1109/NANO.2017.8117338.

841 24. Chang, W.-Y., Huang, W., Kim, J., Li, S. & Jiang, X. Candle soot nanoparticles-

842 polydimethylsiloxane composites for laser ultrasound transducers. *Appl. Phys. Lett.* **107**, 161903
843 (2015).
844 25. Faraz, M., Abbasi, M. A., Sang, P., Son, D. & Baac, H. W. Stretchable and Robust Candle-Soot
845 Nanoparticle-Polydimethylsiloxane Composite Films for Laser-Ultrasound Transmitters.
846 *Micromachines* **11**, 631 (2020).
847 26. Wu, S. *et al.* Superhydrophobic photothermal icephobic surfaces based on candle soot. *Proc.*
848 *Natl. Acad. Sci.* **117**, 11240–11246 (2020).
849 27. Zhang, B., Duan, J., Huang, Y. & Hou, B. Double layered superhydrophobic PDMS-Candle soot
850 coating with durable corrosion resistance and thermal-mechanical robustness. *J. Mater. Sci.*
851 *Technol.* **71**, 1–11 (2021).
852 28. FDA. Marketing Clearance of Diagnostic Ultrasound Systems and Transducers - Guidance for
853 Industry and Food and Drug Administration Staff. (2023).
854 29. Palanker, D., Vankov, A., Huie, P. & Baccus, S. Design of a high-resolution optoelectronic retinal
855 prosthesis. *J. Neural Eng.* **2**, S105 (2005).
856 30. Pisauro, M. A., Dhruv, N. T., Carandini, M. & Benucci, A. Fast Hemodynamic Responses in the
857 Visual Cortex of the Awake Mouse. *J. Neurosci.* **33**, 18343–18351 (2013).
858 31. Provansal, M. *et al.* Functional ultrasound imaging of the spreading activity following
859 optogenetic stimulation of the rat visual cortex. *Sci. Rep.* **11**, 12603 (2021).
860 32. Bhuckory, M. B. *et al.* Cellular migration into a subretinal honeycomb-shaped prosthesis for
861 high-resolution prosthetic vision. *Proc. Natl. Acad. Sci. U. S. A.* **120**, e2307380120.
862 33. Wang, B.-Y. *et al.* Electronic photoreceptors enable prosthetic visual acuity matching the natural
863 resolution in rats. *Nat. Commun.* **13**, 6627 (2022).
864 34. Van Den Berg, T. J. T. P. & Spekreijse, H. Near infrared light absorption in the human eye media.
865 *Vision Res.* **37**, 249–253 (1997).
866 35. Li, Y. *et al.* Optically-generated focused ultrasound for noninvasive brain stimulation with
867 ultrahigh precision. *Light Sci. Appl.* **11**, 321 (2022).

36. Du, X. *et al.* Lead halide perovskite for efficient optoacoustic conversion and application toward high-resolution ultrasound imaging. *Nat. Commun.* **12**, 3348 (2021).
37. Noimark, S. *et al.* Polydimethylsiloxane Composites for Optical Ultrasound Generation and Multimodality Imaging. *Adv. Funct. Mater.* **28**, 1704919 (2018).
38. Qiang, Z., Zhang, Y., Groff, J. A., Cavicchi, K. A. & Vogt, B. D. A generalized method for alignment of block copolymer films: solvent vapor annealing with soft shear. *Soft Matter* **10**, 6068–6076 (2014).
39. Duangkanya, K., Kopwitthaya, A., Chanhorm, S. & Infahsaeng, Y. Oxygen plasma treatment time induced hydrophilicity of polydimethylsiloxane (PDMS) thin films for liquid lenses application. *Mater. Today Proc.* **65**, 2442–2445 (2022).
40. Cheng, J.-X. *et al.* Millimeter-deep micron-resolution vibrational imaging by shortwave infrared photothermal microscopy. *Res. Sq.* rs.3.rs-3449548 (2023) doi:10.21203/rs.3.rs-3449548/v1.
41. Chen, P. *et al.* Acoustic characterization of tissue-mimicking materials for ultrasound perfusion imaging research. *Ultrasound Med. Biol.* **48**, 124–142 (2022).
42. Orhan, E. *et al.* Genotypic and Phenotypic Characterization of P23H Line 1 Rat Model. *PLOS ONE* **10**, e0127319 (2015).
43. Thoreson, W. B. & Ulphani, J. S. Pharmacology of selective and non-selective metabotropic glutamate receptor agonists at L-AP4 receptors in retinal ON bipolar cells. *Brain Res.* **676**, 93–102 (1995).
44. Yger, P. *et al.* A spike sorting toolbox for up to thousands of electrodes validated with ground truth recordings in vitro and in vivo. *eLife* **7**, e34518.
45. Rossant, C. *et al.* Spike sorting for large, dense electrode arrays. *Nat. Neurosci.* **19**, 634–641 (2016).
46. Morisset, C. *et al.* Retinal functional ultrasound imaging (rfUS) for assessing neurovascular alterations: a pilot study on a rat model of dementia. *Sci. Rep.* **12**, 19515 (2022).
47. Bercoff, J. *et al.* Ultrafast compound doppler imaging: providing full blood flow characterization.

IEEE Trans. Ultrason. Ferroelectr. Freq. Control **58**, 134–147 (2011).

48. Montaldo, G., Tanter, M., Bercoff, J., Benech, N. & Fink, M. Coherent plane-wave compounding for very high frame rate ultrasonography and transient elastography. *IEEE Trans. Ultrason. Ferroelectr. Freq. Control* **56**, 489–506 (2009).

49. Demene, C. *et al.* Spatiotemporal Clutter Filtering of Ultrafast Ultrasound Data Highly Increases Doppler and fUltrasound Sensitivity. *IEEE Trans. Med. Imaging* **34**, 2271–2285 (2015).